ORNL/TM-2018/753

Crashworthiness Models for Automotive Batteries

A Report on the Department of Energy Project 2088-A031-15 for the National Highway Traffic Safety Administration (NHTSA), an Agency of the U.S. Department of Transportation.

Sergiy Kalnaus
Hsin Wang
Srdjan Simunovic
Abhishek Kumar
Sarma Gorti
Srikanth Allu
John A. Turner (PI)

January 2018

OAK RIDGE NATIONAL LABORATORY
MANAGED BY UT-BATTELLE FOR THE US DEPARTMENT OF ENERGY

Computational Sciences and Engineering Division (CSMD)
Materials Science and Technology Division (MSTD)

Crashworthiness Models for Automotive Batteries

A Report on the Department of Energy Project 2088-A031-15
for the
National Highway Traffic Safety Administration (NHTSA)
an Agency of the
U.S. Department of Transportation (DOT)

Sergiy Kalnaus
Hsin Wang
Srdjan Simunovic
Abhishek Kumar
Sarma Gorti
Srikanth Allu
John A. Turner (PI)

Date Published:
January 2018

Prepared by
OAK RIDGE NATIONAL LABORATORY
Oak Ridge, TN 37831-6283
managed by
UT-BATTELLE, LLC
for the
US DEPARTMENT OF ENERGY
under contract DE-AC05-00OR22725

Crashworthiness models for automotive batteries.

Report on the Department of Energy Project 2088-A031-15 for the National Highway Traffic Safety Administration (NHTSA), an Agency of the U.S. Department of Transportation.

Sergiy Kalnaus, Hsin Wang, Srdjan Simunovic, Abhishek Kumar, Sarma Gorti, Srikanth Allu, John A. Turner (PI).

Summary

Safety is a key element of any device designed to store energy, particularly of electrochemical batteries, which convert energy of chemical reactions to electrical energy. Safety considerations are especially important when applied to large automotive batteries designed for propulsion of electric vehicles (EV). The high amount of energy stored in EV battery packs translates to higher probability of fire in case of severe deformation of battery compartment due to automotive crash or impact caused by road debris. While such demand for safety has resulted in heavier protection of battery enclosure, the mechanisms leading to internal short circuit due to deformation of the battery are not well understood even on the level of a single electrochemical cell. Moreover, not all internal shorts result in thermal runaway, and thus a criterion for catastrophic failure needs to be developed.

This report summarizes the effort to pinpoint the critical deformation necessary to trigger a short via experimental study on large format automotive Li-ion cells subjected to large deformations as those occurring in deformation of battery module or pack. Mechanical properties of cell components were determined via experimental testing and served as input for constitutive models of Finite Element (FE) analysis. It has been rationalized that long-range stress fields occurring in spherical indentation of battery modules would trigger different deformation and failure scenarios compared to indentation of a single cell supported by a rigid flat surface. In order to investigate large deformations characteristic of battery module, a custom experimental set up has been built where the pouch cell was deformed against a compliant backing, which was represented by a ballistic clay. Experiments were also conducted on deformation of stacks of 10 pouch cells, - configuration representing half-module in Ford Focus EV battery pack without cooling plates and structural components. Comparison of the results shows promise for the compliant backing setup for safety evaluation of battery cells under more realistic conditions compared to indentation of single cell against undeformable backing where compression and electrode particle penetration through separator could be the major mechanism for short circuit.

Contents

Introduction

Li-ion batteries for mobile electronic devices and appliances are usually in the form of single cells or small cell packs, where mechanical abuse could occur by handling of the cells during transportation and storage. The end-users are not subjected to risks from mechanical abuse under normal conditions. Although the once in several million chance of self-induced internal short circuit event has always been a potential safety concern, recent advances in cell chemistry, safer electrolytes, separators [1], and battery management system (BMS) have kept this issue a low priority. The emphasis on more specific power in mobile devices has led to current Li-ion cells to share the same designs with a light-weight pouch cell and thinner layers of current collectors and separators. They are vulnerable to mechanical abuses such as crushing, bending and dropping. For electric vehicle (EV) applications, the same designs for small cells were simply scaled up in dimensions to make large format cells. The larger cells carry significantly more energy and inherit the same mechanical abuse-intolerant characteristics of their smaller counterparts. For the same mechanical damage and same state of charge (SOC), a larger cell is more likely to go to thermal runaway because it has higher capacity and more current can flow through the short circuit spot to trigger thermal runaway. With the increasing number of electrical vehicles entering the active fleet, battery safety has become an important issue [2]. In addition to the safety of handling and transporting the cells, the EV users can be directly affected by the mechanical abuses and failure of the batteries. In order to avoid mechanical damage, the cell packs are located in the crush-safe zones and protected by extra armors. However, severe accidents can still lead to mechanical deformation of the cells, short circuit in the cells and potential thermal runaway.

A damage tolerant design of batteries rests upon detailed understanding of the processes leading to failure and the ability to model such processes. Such understanding is especially critical in the case of battery pack designs for electric vehicles. Current lack of such understanding is not surprising, considering the difficulty of the problem, which combines mechanics of battery response to crush loading with electrical and chemical behavior. While there are federal safety regulations [3] and industry standards related to battery safety [4, 5], they mostly address passive safety measures such as electrolyte spillage or disconnection of the high voltage battery pack in case of malfunction.

A number of tests on safety of Li-ion cells under mechanical abuse have been developed over the years, with probably the most well-known being the “nail penetration tests” standardized by SAE as J2462 [6]. Majority of the recommendations for abuse testing of automotive batteries can be found in “Abuse Test Manual for Electric and Hybrid Electric Vehicle Applications” released by Sandia National Laboratories [7]. It should be mentioned that unavoidable manufacturing variability results in difficulties in the determination of location of short circuit and formulation of criteria for thermal runaway. In addition, most of the tests are destructive, and post-mortem analysis cannot supply definitive evidence regarding the origin of the short. Localized high joule heating within the internal short circuit can trigger a chain of exothermic reactions that can raise the temperature enough to create combustion of flammable gases in the cell (thermal runaway).

This report summarizes progress in development of an experiment for out-of-plane indentation of pouch cells constrained in the manner representative of automotive battery packs. Such deformation involves large strains and a different failure mode compared to traditionally practiced single-cell indentation on a rigid support. Complementary to these experiments, we study deformation of battery separators alone, subjected to a similar deformation mode, in order to determine the critical strain for failure. The findings are supported by finite element (FE) modeling of indentation of battery modules and strain distribution in battery separators.

1. Experiments

Various studies can be found in the literature on mechanical testing of Li-ion cells [8]. For small cells used in mobile devices, UL 1642 [9] describes four mechanical abuse tests that the cells with less than 5 grams of metallic lithium must pass, including crushing, impact, shock and vibration. These tests mainly focus on possible mechanical abuses during the transportation and storage of the cells. The passing criteria for these tests are: no fire and no explosion. For self-induced internal short circuit, there is no standard test. Most techniques were developed to simulate an internal short circuit at a single layer due to manufacturing defects. Alternative ways to simulate such a defect require opening a live cell and putting a foreign object inside the cell [10] or embedding an "instigator" inside the cell [11, 12]. These methods work well in a laboratory environment and are not practical in production and for in-service evaluations. Nail penetration [13] or single-side indentation [14] usually can cause extensive damage to the cell before the short circuit event. Efforts to develop mechanical pinching [15] and torsion [16] tests have been made to modify the simple nail penetration or mechanical indentation tests in order to induce a small short circuit spot deep inside the cell. It is important to point out that none of the above tests can perfectly mimic an actual internal short circuit event. They can be treated as cell safety evaluation methods and are more effective in comparing cell-to-cell and design differences.

For large format cells, no formal mechanical abuse test standards or internal short circuit tests are available, although many efforts can be found in the literature [17-19]. Mechanical testing to simulate damage in a crash situation is fundamentally different from internal short circuit simulations. These tests need to cover various externally induced mechanical deformations. In most cases, the damage involves multiple layers and in some cases multiple cells. It is common to conduct mechanical deformation tests until battery failure (usually a voltage drop) is detected. The final results are multiple layer short circuit and rapid local heating. Even with the minimal capacity, the resulting mechanical damage and localized joule heating make it very difficult to pin-point the final failure mechanism. In most accidents involving EVs, the field data are very hard to obtain, and are totally destroyed in the case of vehicle fire. In addition, the vast majority of experiments on mechanical abuse involves testing single cells on rigid foundation, which triggers significant compressive strains and stresses, as well as the possibility for electrode particle penetration through the separator. The latter was standardized into the "mix penetration strength" requirement for battery separators [20]. Deformation inside the battery pack however triggers larger strains and results in a different strain distribution due to coordinated response of multiple cells in a battery.

Studying the behavior of automotive pouch cells under conditions representing the deformation inside the battery pack during vehicle crash is the primary goal of this work. Development of an experimental setup that would allow such study was one of the major tasks. We simulate experimentally an out-of-plane penetration of a spherical rigid object into the pouch cell, allowing for large deformations by substituting the rigid support with a specially designed flexible backing. In addition, we study deformation of battery separators alone in a similar configuration in order to obtain details of strain distribution in anisotropic separators and in order to collect data on failure strain in separators. Among all of the cell components, separators were chosen for such detailed study since they are considered to be the most critical safety part of cell design, i.e. mechanical failure of the separator is a necessary condition for contact between electrodes and internal short circuit.

1.1. Development of the experimental setup for large deformation of cells

In automotive battery packs composed of pouch cells (e.g. the pack in Chevrolet Volt or Ford Focus EV) the cells are placed in stacks (modules) and are contained under pressure applied by external platens. During the out-of-plane deformation, the strain is distributed over many cells and therefore the experiments should involve several cells stacked in a string. As a basic unit, we chose half of the Ford Focus EV battery module. The full module contains 20 cells, as shown in Fig. 1 (for battery disassembly procedure please see Appendix B).

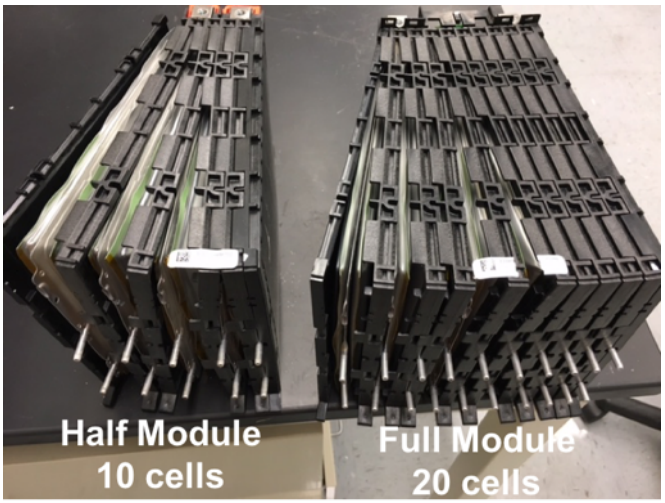

Fig. 1. Cells in Ford Focus EV module and half-module as removed from the battery pack

Deformation by a rigid sphere in the direction perpendicular to the cell plane was considered in the current investigation. In order to replicate the conditions inside the battery module, two experimental setups were created. In one, the cells were sandwiched between two aluminum plates (5 mm thick) and held in place by tightening screws which applied pressure through aluminum brackets (Fig. 2(a)). The top plate had a central circular opening to accommodate the spherical indenter of 1-inch diameter. In the second setup, a single cell was retained and the remaining 9 cells in the half-module were replaced by a deformable backing. We used an approach similar to ballistic testing of body armor and used ballistic clay (Roma plastilina) to represent the remaining portion of the module. The box (Fig. 2(b)) to contain the ballistic clay was designed to accommodate the Ford Focus EV cell with dimensions 150 mm x 200 mm supported by 55 mm-thick layer of Roma plastilina. With the pouch cell thickness being 5.5 mm, this layer approximates 10 cells, as in half-module. The box was made of aluminum alloy and was designed to withstand the weight of the clay along with additional loads coming from experimental indentation, as well as for easy disassembly following the experiment. The top cover of the box had a circular opening for the indenter and was pressed against the pouch cell surface in order to avoid any warping or folding in the cell. Different grades of ballistic clay were obtained for the experiments, with grade 1 being the most compliant and grade 4 being the stiffest.

The setup with ballistic clay was designed to accomplish two major goals: i) aid in investigation of cell deformation and failure; ii) contribute to development of a new safety testing procedure which eliminates the necessity to deform the whole battery module, which typically presents serious safety concerns and requires elaborate protection techniques. When the rest of the battery module is substituted with representative deformable medium, only one cell is subjected to deformation and experiences internal short circuit in the event of failure, which decreases the severity of thermal runaway. It should be mentioned that in the current investigation the cells were

received and tested in completely discharged state, which enabled investigation of mechanical response and failure due to external loading without triggering destructive fire events.

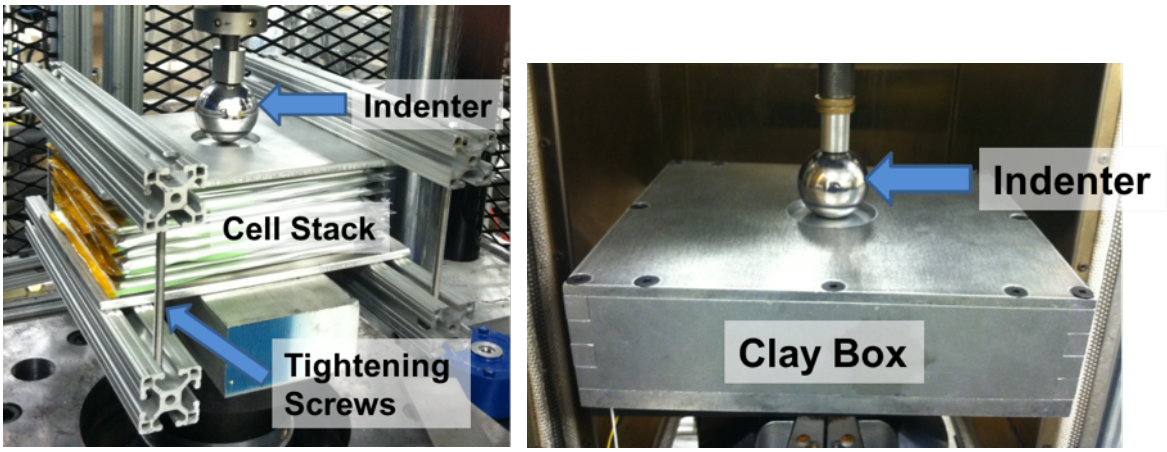

(a)¶ ¶ (b)

Fig. 2. Experimental setup to replicate deformation in battery module: (a) compressed stack of 10 pouch cells; (b) pouch cell on ballistic clay.

1.2. Experiments on cell stacks and cells on compliant backing

An MTS servo-hydraulic loading frame was used in the experiments involving both 10-cell stacks and cell-on-clay configurations. All the experiments were done with an indenter of 1-inch diameter. Experiments were performed under displacement control and the crosshead speed was maintained at 127 μm/s. All the tests were performed at room temperature and in ambient air. The cells from the Ford Focus EV were obtained in fully discharged condition. In order to detect the internal short circuit and correlate it with critical deformation, a small current was passed through the cell in order to slightly increase its potential; the internal short circuit would then correspond to a potential drop during the experiment. Potential was monitored in the two top cells in the 10-cell stack setup (Fig. 3(a)) and in the cell supported by the ballistic clay (Fig. 3(b)). Data acquisition was handled using LabView software by National Instruments, which was configured for simultaneous recording of potential and force as a function of time.

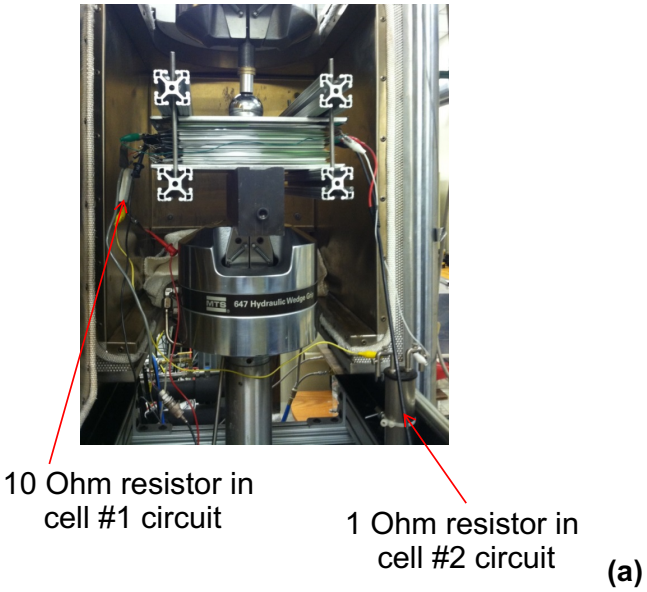

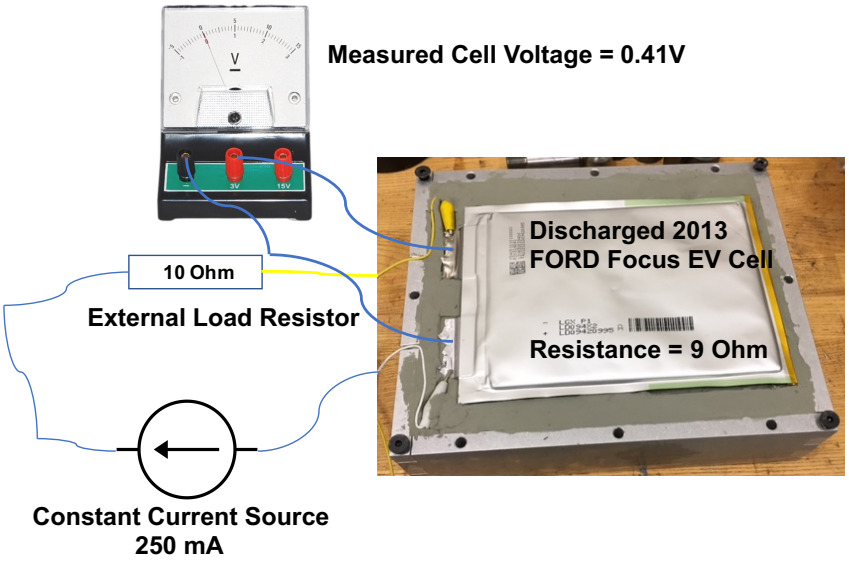

(b)

Fig. 3. Experimental setup showing electrical connections: (a) 10-cell stack; (b) single cell on ballistic clay.

The results of indentation of the 10-cell stacks are shown in Fig. 4. While all three experiments were performed under identical conditions, there is apparent spread in the observed behavior of the cells. Since the potential of the two cells on the top was monitored, a judgement can be made whether the failure in the cells evidenced by the potential drop occurs simultaneously in both cells or there is a certain delay between the short circuit occurring in the top cell and the one underneath it. The results show that both scenarios are possible. The failure in the two top cells can occur nearly simultaneously or have a pronounced delay, as in Fig. 4(b) (the delay between the failure of the top two cells in the stack was 1.6 s in this experiment). It should be mentioned that the data acquisition rate was maintained at 100 Hz which enabled accurate detection of the potential drop inside the cell as evidence of internal short circuit.

Overall, the load-displacement curves look similar in all three tests, with the loads at failure ranging from 30 kN to 39 kN. It should be noted that the critical displacement of the indenter corresponding to the failure of the cells is fairly consistent and is close to 10 mm. The other major observation is that the drop in potential corresponding to the short circuit is not associated with the load drop which would indicate complete mechanical failure of the cell. The point of potential drop in the second cell corresponds to a change in the slope of the load-displacement curve; potential drop in the first cell was not accompanied by any noticeable change in stiffness of the cell stack. This observation contradicts findings of experiments on rigidly supported single cells that the short circuit (potential drop) in the cell always coincides with load drop indicative of the cell failure [17].

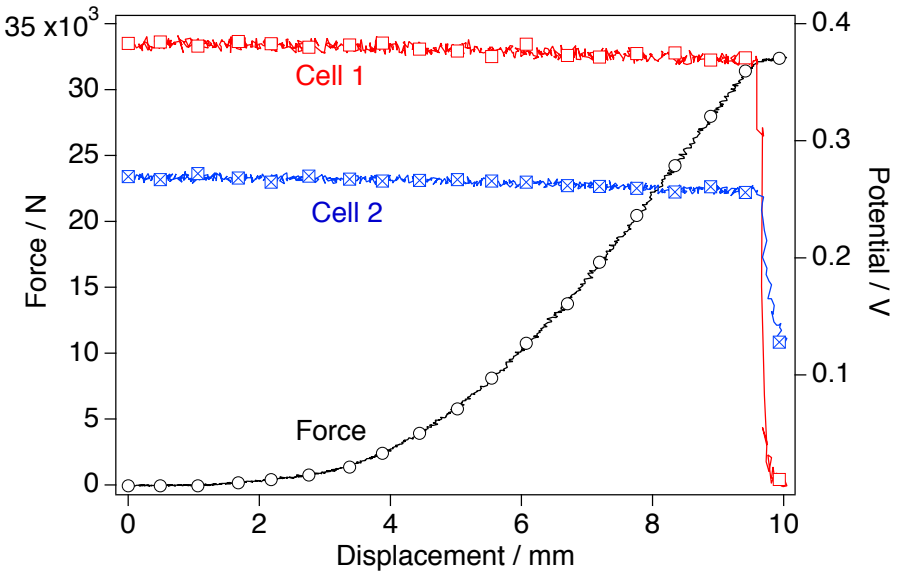
35 x10^3
30
25
20
15
10
5
0
Force / N
0.4
0.3
0.2
0.1
Potential / V
Cell 1
Cell 2
Force
0
2
4
6
8
10
Displacement / mm

(a)

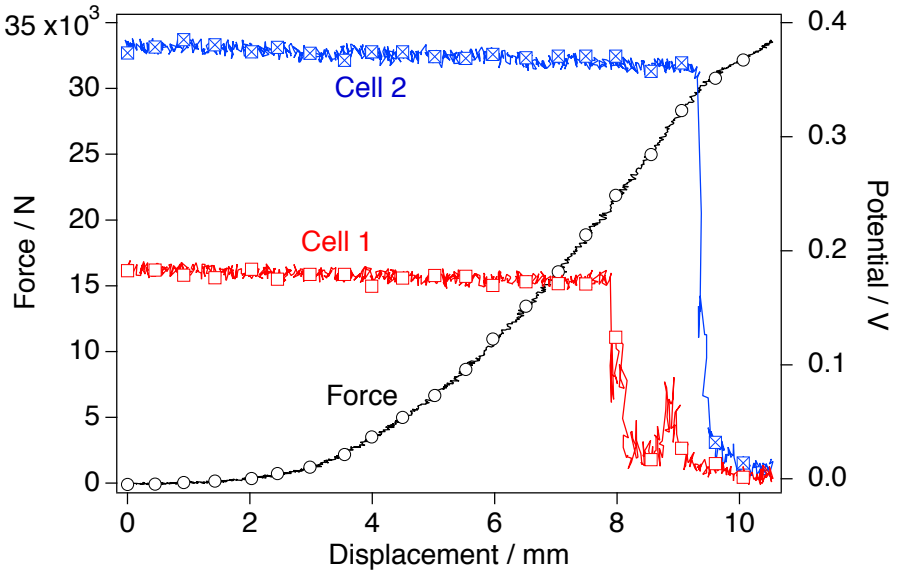
35 x10^3
30
25
20
15
10
5
0
Force / N
0.4
0.3
0.2
0.1
0.0
Potential / V
Cell 2
Cell 1
Force
0
2
4
6
8
10
Displacement / mm

(b)

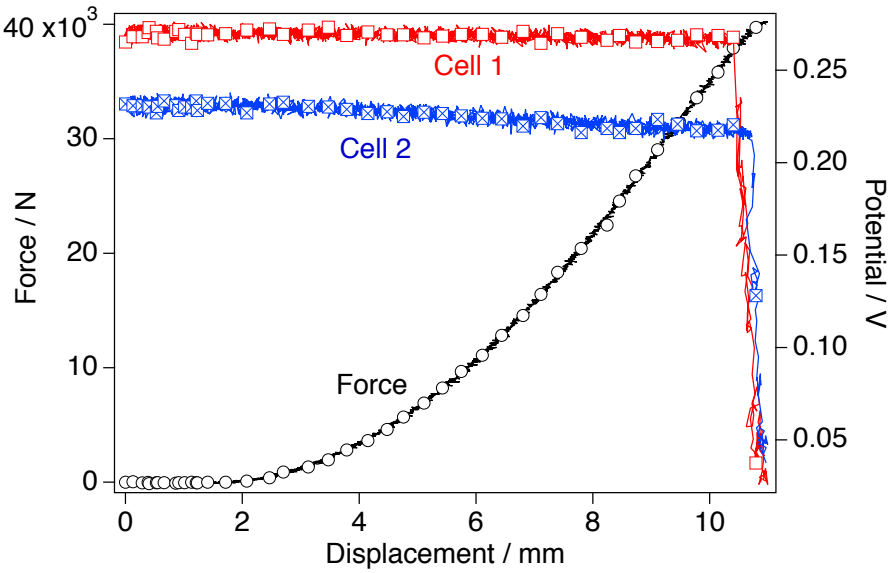

Fig. 4. Results of experiments on 10-cell stack under out-of-plane indentation

Ballistic clay used in the current work comes in four different grades with decreasing pliability from grade 1 to grade 4. Ideally, the stiffness of the clay should match that of the cell stack. Comparison of different clays revealed, however, rather little influence on the stiffness of the system. It was determined that even the hardest clay (grade 4) results in a stiffness considerably lower than that of the 10-cell stack, as shown in Fig. 5.

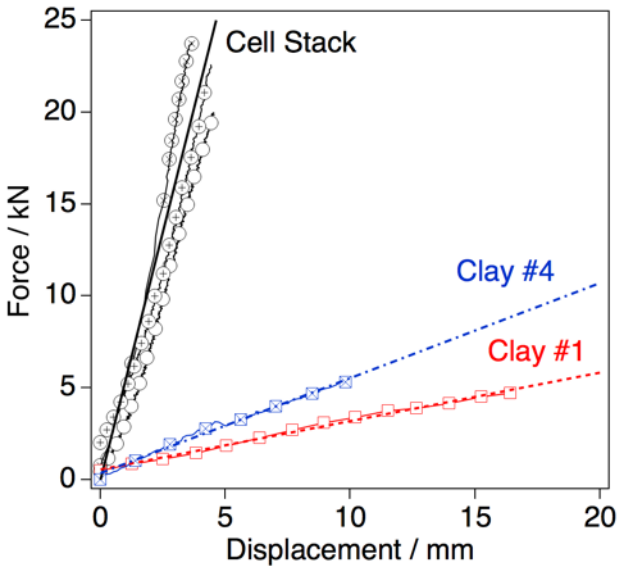

Fig. 5. Comparison of stiffness between cell on clay and 10-cell stack configurations

Despite the difference in stiffness, the response was qualitatively the same for the two arrangements. The load-displacement response together with monitored potential of a single pouch cell supported by ballistic clay is shown in Fig. 6. It can be noted that, similarly to the case of cell stack, the internal short circuit (potential drop) coincides with a small change of stiffness (d*P*/d*z*) as opposed to a substantial load drop indicative of major internal failure. This feature

consistently distinguishes failure under large displacements due to flexible substrate from that of a cell resting on an undeformable support.

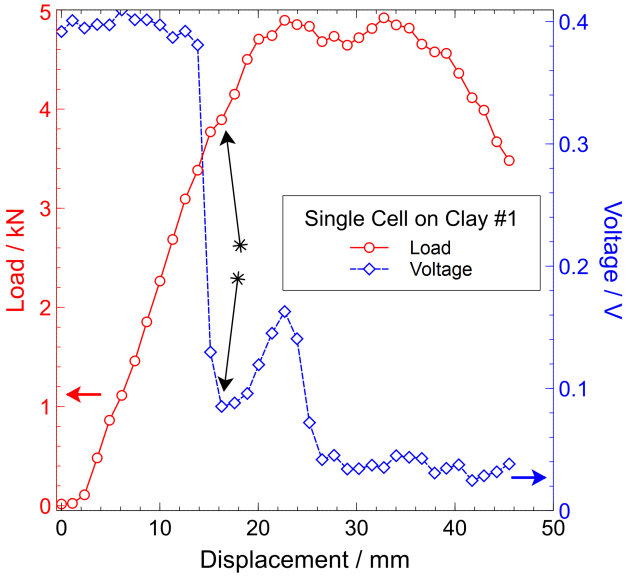

Fig. 6. Deformation and failure under spherical indentation of pouch cell supported by ballistic clay.

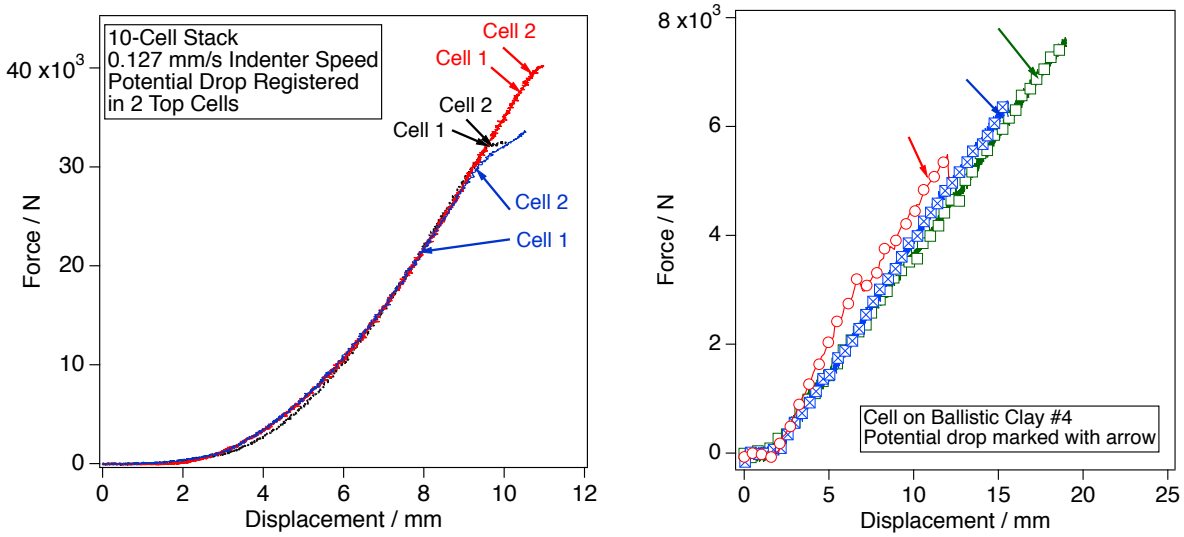

(a) (b)

Fig. 7. Load-displacement curves representing spherical indentation of (a) 10-cell stack; (b) single cell on compliant support.

Comparison between the load-displacement curves of 10-cell stacks and cell on ballistic clay (grade 4) setup can be seen in Fig. 7. The moments in loading history where voltage drop in cells was recorded are indicated by the arrows (potential in two top cells was monitored in the 10-cell stack setup). As can be seen, the failure of a single cell does not trigger noticeable changes in stiffness; this can be observed in the case of “cell-on-clay” setup as well as in the stack of cells, where the reduction in stiffness can be observed only after the failure in the second cell. Significant, more than an order of magnitude, difference in force corresponding to cell failure can be noted, which is expected considering difference in stiffness between ballistic clay and stack of

pouch cells. Critical displacement of the indenter corresponding to the internal short circuit is also different between the two loading cases: 9.89±0.7 mm in case of 10-cell stack and 14.43±3.32 mm in case of cell on clay arrangement. We, however, believe that the two loading cases can be correlated via the critical strain for failure, as discussed in the next section.

All of the cells failed by a single major crack oriented perpendicular to the cell tabs. This direction corresponds to the winding direction of the jelly-roll during the pouch cell assembly, and correspondingly, to the machine direction (MD) of the battery separator. Examples of the failure patterns are shown in Fig. 8 together with the machine and transverse directions of separator (MD and TD respectively, indicated by arrows). The implications of anisotropy of separator mechanical properties are discussed in detail in the next section.

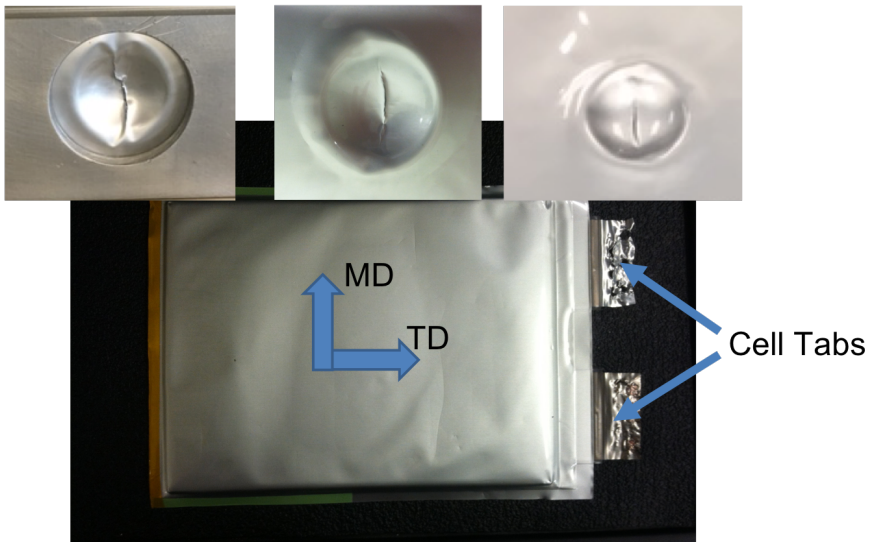

Fig. 8. Orientation of failure cracks on the pouch cells under spherical indentation

In order to get insight into deformation of a complete battery module and compare the results against model predictions, an additional indentation was performed on a Nissan Leaf module, which contains 4 pouch cells. For details of Nissan Leaf Li-ion battery pack and module teardown please see Appendix B. The module was tested in “as received” condition; no modifications were done apart from discharging it from nominal 6V in order to perform experiment safely. Indentation was done by a 2-inch diameter sphere at 0.1 inch/min crosshead speed (Fig. 9).

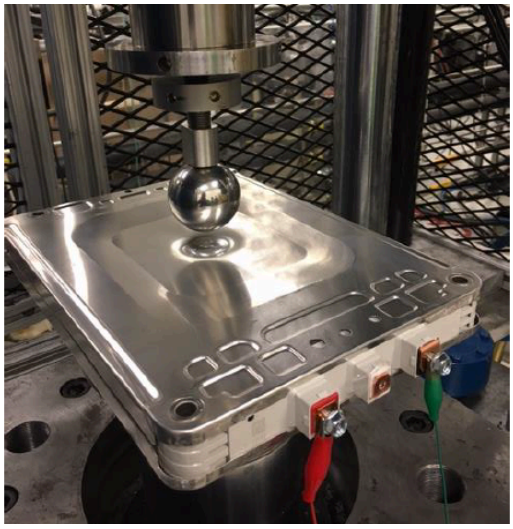

Fig.9. Spherical indentation of Nissan Leaf module

1.3. Mechanical behavior of battery separators under biaxial deformation

In order to gather more information on the separator behavior, biaxial mechanical experiments were performed representing conditions closer to those involved in cell or battery deformation under out-of-plane impact by a rigid object. The following setup was assembled for this purpose (Fig. 10). The load frame was equipped with a 100 lbs load cell (445 N). The circular sample of separator was placed between two stainless-steel 304L flanges. The edges of the inner flange opening were chamfered and smoothed; in addition, rubber gaskets were placed between the flanges to avoid any tearing of the separator by the steel. The nuts holding the flanges were hand tightened to avoid applying excess pressure to the perimeter of the sample. This provided enough force to keep the separator from pulling out of the flanges, and at the same time avoided over-tightening the flanges.

The deformation was imparted on the specimen by moving the polished hardened steel ball upward, thus creating biaxial stretch of the separator sample. The approach is reminiscent of the deep drawing tests (or dome tests) in sheet metal forming research. Spheres of three different diameters were used: 1 inch (25.4 mm), 2 inch (50.8 mm) and 2.5 inch (63.5 mm). The steel balls were mirror polished by the supplier (McMaster-Carr Supply Co). In addition, they were sprayed with Teflon anti-friction coating. The ball was supported in the loading setup by the concave surface of the coupler; the latter was threaded to the load cell. There was no rigid attachment between the sphere and the load train of the machine- this arrangement avoided any bending or torsion. The speed of the ball was maintained at 0.008 inch/s (0.2 mm/s) in all of the experiments. 24 samples were tested in total with two different types of commercial separators: Celgard 2325 and Celgard 2075. Celgard 2325 consists of a Polyethylene (PE) layer sandwiched between two Polypropylene (PP) layers, while Celgard 2075 is a single-layer PP porous membrane.

Table 1: Properties of separators

	Composition	Thickness, μm	Porosity, %	Pore size, μm
Celgard 2325	PP/PE/PP	25	39	0.028
Celgard 2075	PP	20	48	0.037

The basic parameters of the separators are given in Table 1. The microstructure of as-received and deformed separators was observed with Hitachi S4800 field emission scanning electron microscope (FE-SEM). Pore size of PP2075 was measured using SEM images of separator with the help of ImageJ software and the average major radius of the pores is reported in Table 1. Average pore size of Celgard 2325 was provided by the manufacturer.

The system was equipped with CCD cameras and software Vic3D by Correlated Solutions, for Digital Image Correlation (DIC). In order to create the speckled pattern, the sample was sprayed with stencil permanent ink. All experiments were done at room temperature and in ambient air. Details of the experimental procedures can be found in [21].

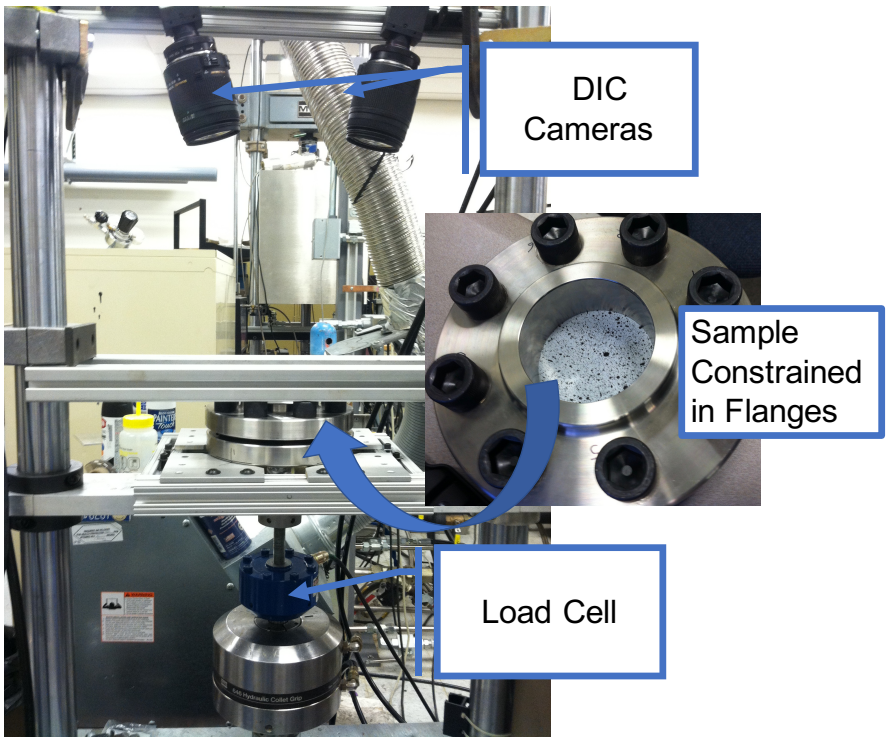

Fig. 10. Setup for biaxial test of battery separators with strain measurements

Both types of separators investigated here failed due to straight cracks always oriented along the machine direction. Examples of the failure pattern are shown in Fig.11 for Celgard 2325 deformed by a 50.8 mm sphere (Fig.11a) and Celgard 2075 deformed by 25.4 mm sphere (Fig.11b).

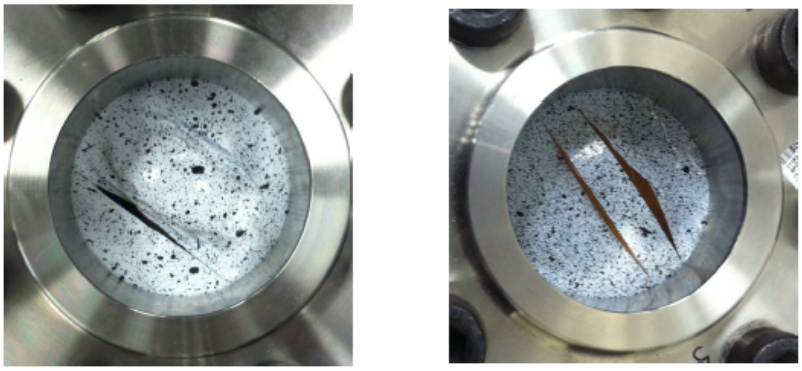

(a) (b)

Fig. 11. Failure pattern of separators under biaxial deformation. (a) Celgard 2325 deformed by 50.8 mm sphere; (b) Celgard 2075 deformed by 25.4 mm sphere.

Microstructure of separators in as-received condition and after biaxial deformation is shown in Fig. 12. It should be noted that porosity in this type of separators is obtained by directional stretch which forms the slit-like pores with thin fibrils aligned with machine direction (MD) and connecting thicker lamellae running along transverse direction (TD). Such procedure is based on process of crazing [22], typical for polymers undergoing tensile deformation, and results in anisotropic properties of the membrane, with strength in MD (direction of stretch and winding

direction in jellyroll fabrication) being significantly higher than strength in TD. Details of separator manufacturing can be found in [23, 24]. Application of large biaxial deformation results in simultaneous extension and formation of new fibrils as well as extension and break up of thick lamellae.

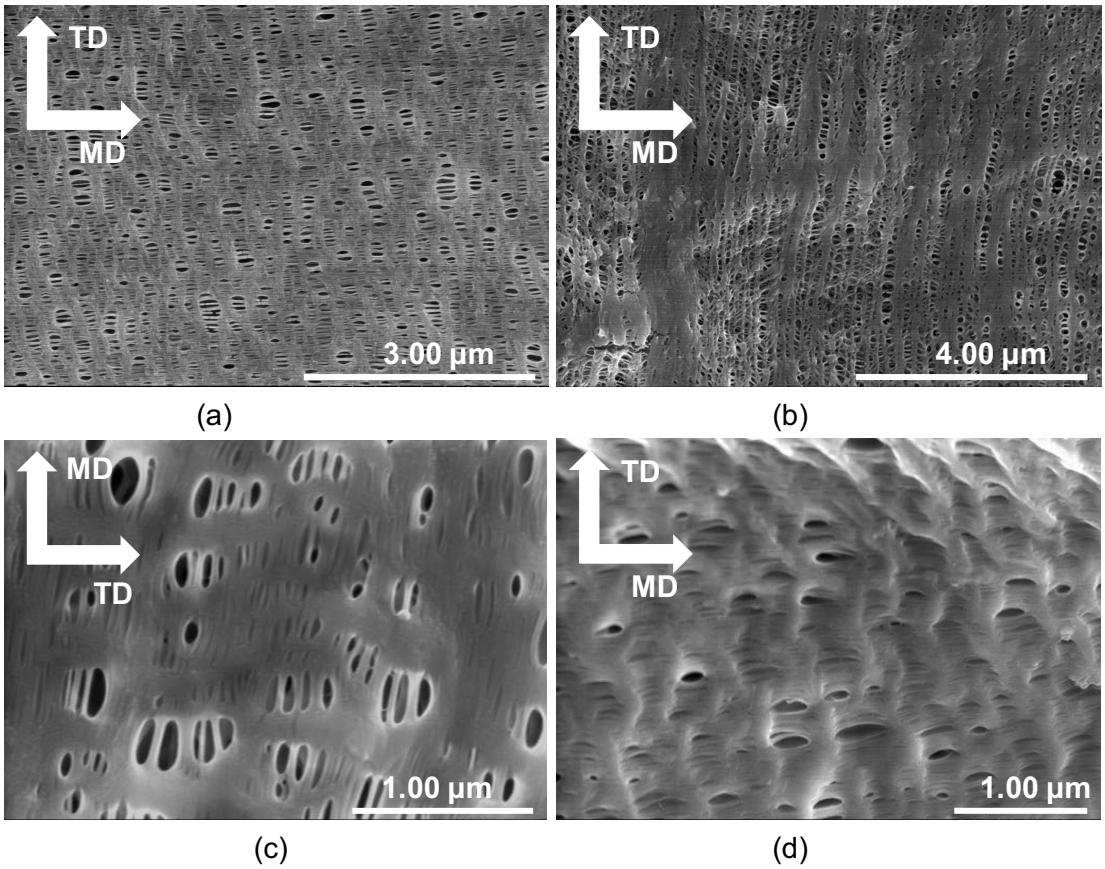

Fig. 12. Microstructure of separators prior (a, c) and after (b, d) biaxial deformation. Celgard 2325 (a, b) and Celgard 2075 (c, d).

Figure 13 shows distribution of first principal strain calculated from captured DIC images during the experiment. Figures 13a and 13b show response of Celgard 2075 and Fig.13c, 13d show the strain distribution in Celgard 2325. Deformations induced by 50.8 mm sphere (Fig.13a, 13c) and by 25.4 mm sphere (Fig.13b, 13d) show symmetrical distribution of maximum principal strain with respect to the sample centerline. Such distribution matches the location of the cracks in the separator. The elongated shape of the maxima of major strain is attributed to anisotropy of mechanical properties of the separator.

It appears that the critical principal strain at failure is very close in both separators regardless of the sphere size. For triple-layer separator Celgard 2325, the necking strain was determined as maximum principal strain of 0.34 ± 0.05. The principal strain at failure for Celgard 2075 was determined as 0.43 ± 0.069 from the current experiments. The thinning of the separator, which we somewhat loosely term as necking here, is evidenced by the formation of semi-transparent bands running along the machine direction; these are indicated by the white arrows in Fig. 13.

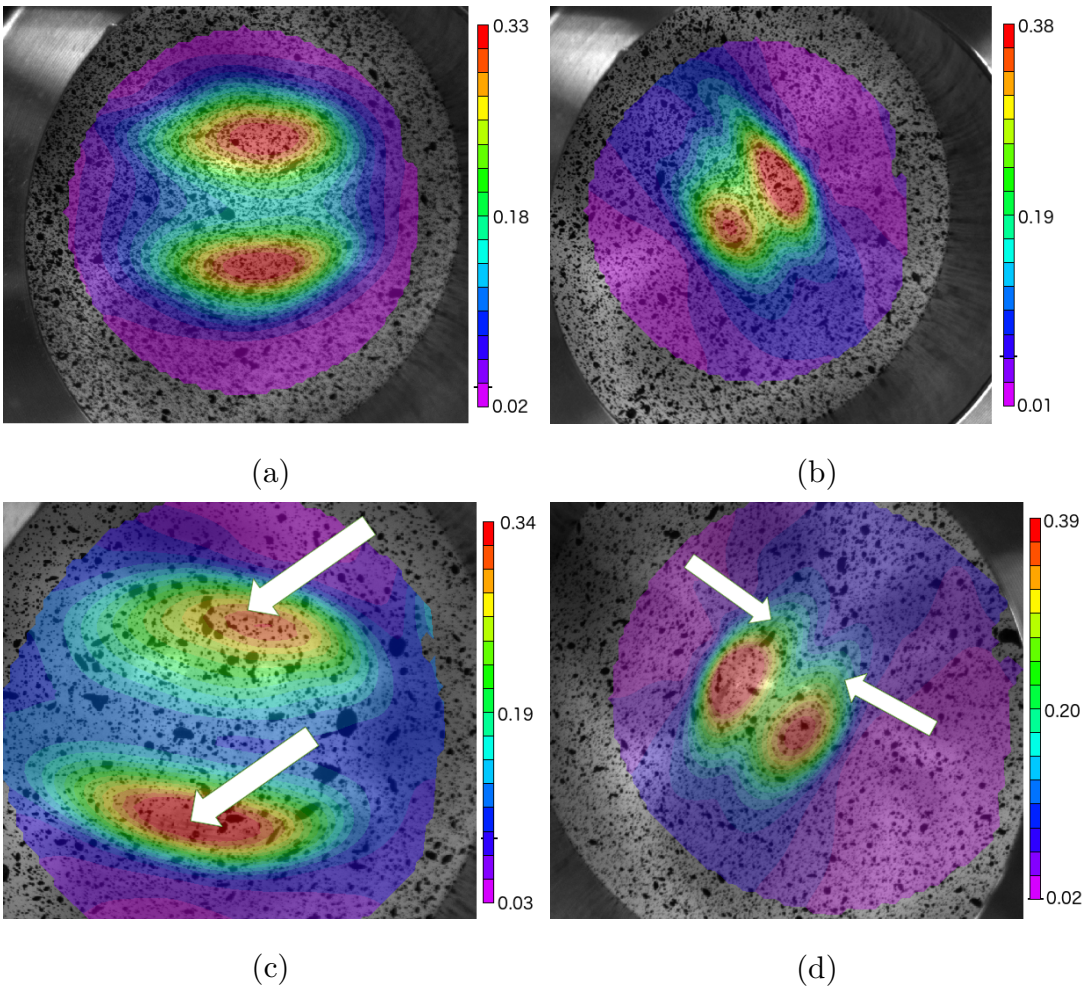

Fig. 13. Distribution of first principal strain in biaxially deformed (a,b) Celgard 2075; and (c,d) Celgard 2325

2. Simulations

Indentation experiments were simulated using the FEM software package LS Dyna [25]. LS Dyna uses an explicit time integration method and is capable of efficiently modeling nonlinearities in material, structure and geometry. The indentation test was conducted with a rigid sphere modeled as an analytical surface moving at a constant speed. Simulations of two case scenarios were performed: indentation of Nissan Leaf battery module (Section 1.2) and biaxial deformation of battery separators (Section 1.3). The purpose for the first simulation was to demonstrate implementation of the layered solid finite element as well as to perform FEA on realistic geometry of the module. Purpose of the second analysis was in establishing predictive simulation for the strain distribution in battery separators utilizing anisotropic model for separator mechanics.

2.1. Material models

Table2: Physical Parameters for various components of a single layer of a battery cell

Component	Thickness (*mm*)	Material Model	Elastic Modulus (*GPa*)	Yield Strength (*GPa*)	Tangent Modulus (*GPa)*
Copper	0.011	MAT-24	110	0.24	0.1
Anode	0.064	MAT-24	0.45	0.04	0.01
Separator	0.024	MAT-24	0.5	0.06	0.05
Cathode	0.080	MAT-24	0.55	0.04	0.01
Aluminum	0.018	MAT-24	70	0.24	0.1

2.2. FE model of battery module

In this section, we describe the Finite Element analysis of the Nissan Leaf module, following the indentation experiment described in Section 1.2. The finite element model for the module is shown in Figure 14. The module consists of aluminum case containing four battery cells. The dimensions of individual cell are 300 X 100 X 6.82 mm. We have used the layered solid element to model individual battery cell. Each battery cell is modelled using 4 layered solid elements, one layered solid element consists of 32 integration points of repeated layers of copper, anode, separator, cathode and aluminum as shown in Figure 14 (b). We can use separate material model at each integration point, material model is selected from Table 2. Mechanical properties for all these components have been taken from [26]. The spherical punch was modeled as a geometrical analytical rigid body. The lower surface of the cell rested on a rigid wall. We prescribed rigid body motion for the sphere and controlled its vertical movement as a linear function of time such that the velocity of sphere in z direction was constant. The contact between the rigid sphere and battery module was modeled as contact-entity feature with a coefficient of friction of 0.3.

In Fig. 15 we show the load displacement curves obtained from experiment and predicted by the FEA. Significant discrepancy between predicted and measured forces can be observed at higher displacements which can be a result of several factors. A better choice of a material model for the electrode material would be desirable to replace the elasto-plastic MAT 24 used in the

current analysis. A crushable foam model (MAT 63) or Mohr-Coulomb (MAT 173) model could be better applicable considering that model for electrode coatings can be based on soil mechanics. Secondly, the simplifications in the finite element model excluded some components in the internal module structure, including the stiff plates separating cells from the module casing. These plates (see Appendix B for more details) are made of stiff plastic-like material with mechanical properties that have not been measured yet. Despite the discrepancy, the results show applicability of the layered solid finite element formulation to the problems where resolution of individual layers in the layered structure (such as battery cells) using solid elements leads to prohibitive increase in the problem size in terms of the number of elements.

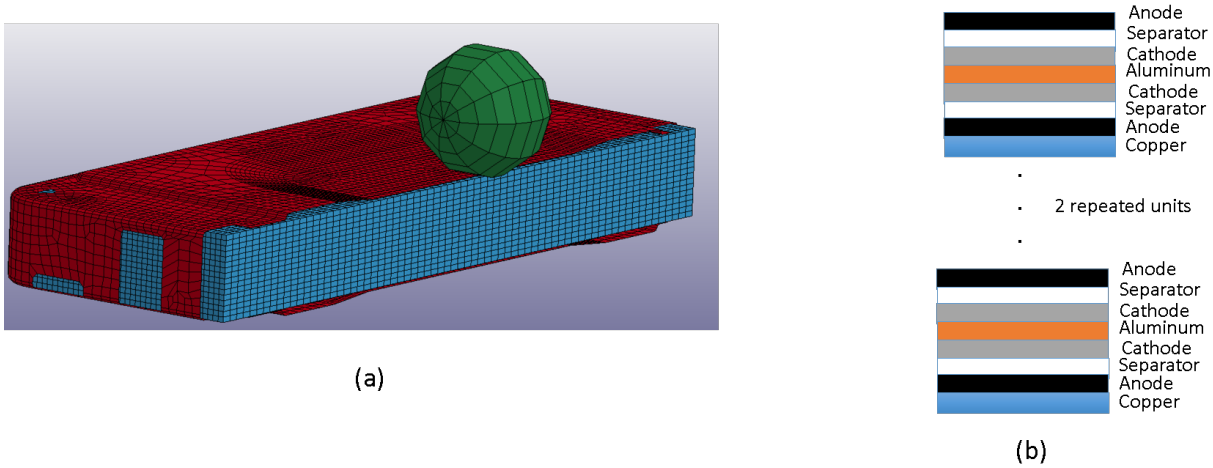

Fig. 14. Finite Element Representation of the Module (a) Layered Solid element (16 elements across the thickness) (b) Schematic of an individual layered solid element. Repeated unit has 8 integration points consisting of anode, separator, cathode, aluminum, cathode, separator, anode and copper

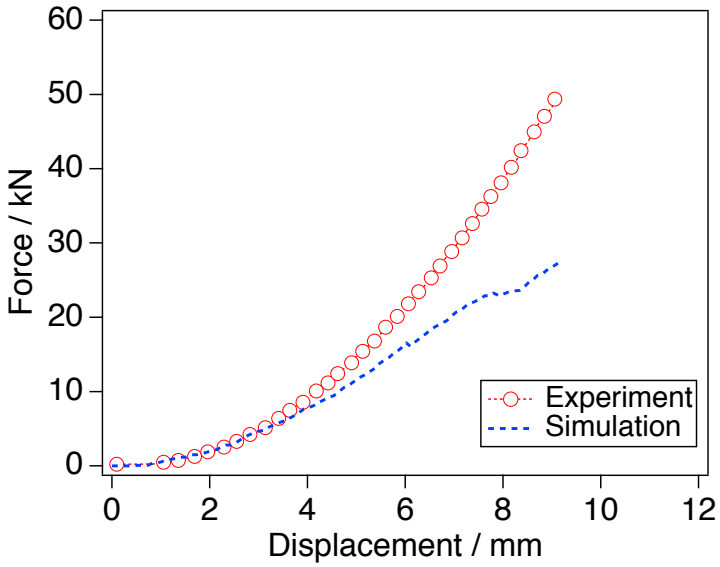

Fig. 15. Load Displacement curve for the module

2.3. Simulations of strain distribution in battery separator

Finite element analysis of stress-strain state in separators subjected to biaxial deformation as described in Section 1.3 has been performed using LS DYNA. Due to directional dependence of polymer separator properties, MAT-36 material model was chosen from library of LS DYNA materials [25, 27]. Since the conditions for biaxial stretching of separator employed in the current investigation are similar to those in sheet metal forming test we assume the validity of such model selection and assume plane stress state for separator. The stress strain curve obtained under tensile test in MD was used as an input for 0^0 curve, while the stress-strain curve in TD (weak direction) was used as an input for 90^0 curve. Due to lack of experimental data from 45^0 tension, a curve corresponding to this direction was calculated as an average of stress-strain data in TD and MD.

Finite element mesh for separator was developed using membrane like shell element (ELFORM=-16 in LS Dyna [25]). The schematic of the mesh along with three different spheres is shown in Fig.16. Thickness for the shell element was same as that of separator (0.025 mm for Celgard 2325 and 0.020mm for Celgard 2075). The radius of the separator membrane was taken as 38 mm, which corresponds to the inner radius of the flanges used to hold the sample. The finite element nodes on the perimeter of the circular membrane were constrained in all the directions; the part of the material that was held in place between the flanges was not included in the model. The sphere in contact with the separator was prescribed a displacement in the downward direction such that its speed was constant throughout the deformation. The sphere was treated as a rigid material and was modeled using contact entity feature in LS Dyna. Contact was treated between these contact entities and the slave nodes in the separator using a penalty formulation. Kinetic friction coefficient between the separator and the metal sphere was chosen as 0.6 in the present simulations. We treat this coefficient as an adjustable parameter and the selected value resulted in a good quantitative match between measured and predicted strains and forces.

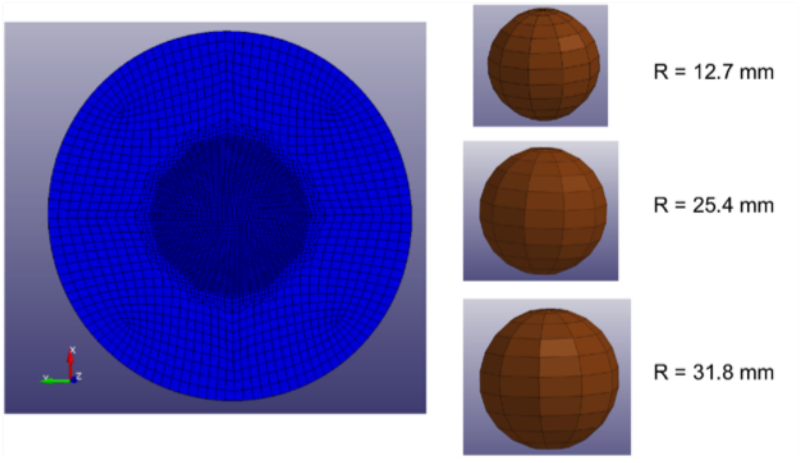

Fig. 16. Mesh of separator along with the spheres of different radii used in biaxial deformation

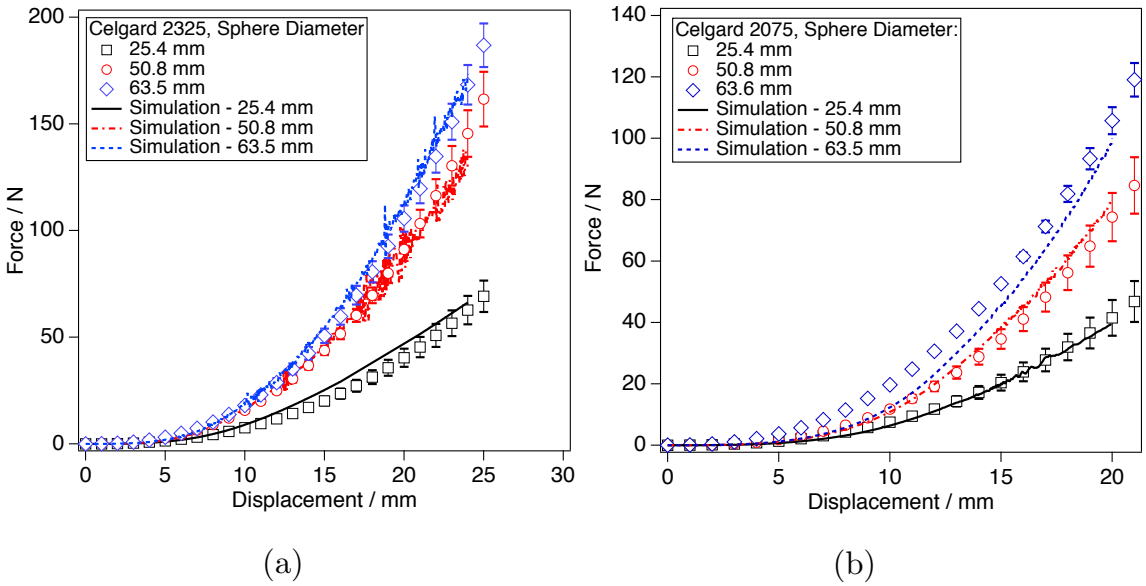

(a) (b)

Fig. 17. Experimental and simulated load-displacement curves for (a) Celgard 2325; (b) Celgard 2075

The load-displacement curves of the separators deformed by the spheres of the three different diameters are shown in Fig.17a for Celgard 2325 and in Fig.17b for Celgard 2075. With the purpose of brevity experimental data points including error bars are shown together with the predictions from numerical simulations. Good agreement between measured and predicted forces and displacements can be observed in Fig.16. As expected the loads required to deform separator depend on the ball diameter, with smaller loads produced by smaller diameter sphere. In addition, the forces resulting from deformation of Celgard 2325 are about two times higher compared to those involved in stretching of Celgard 2075. This could be anticipated since Celgard 2325 is a triple-layer separator with higher thickness.

Distribution of major strain as predicted by simulations is shown in Fig. 18 (a, c) for 25.4 mm indenter and in Fig. 18 (b, d) for 50.8 mm indenter. The strains are shown at 15 mm of vertical displacement of the spherical indenter - an average travel corresponding to the first appearance of transparent stretch regions (necking) in separator. Comparison with Fig. 13 reveals good match of the maximum strain value (~35%) between measured and predicted strains. At the same time, while the separator properties results in oval-shaped contours of the major strain in Fig. 18, highly localized concentration of strain is missed in numerical predictions. It can be seen however that the locations of the strain maxima aligned along the machine direction correlate very well with the experimental observations.

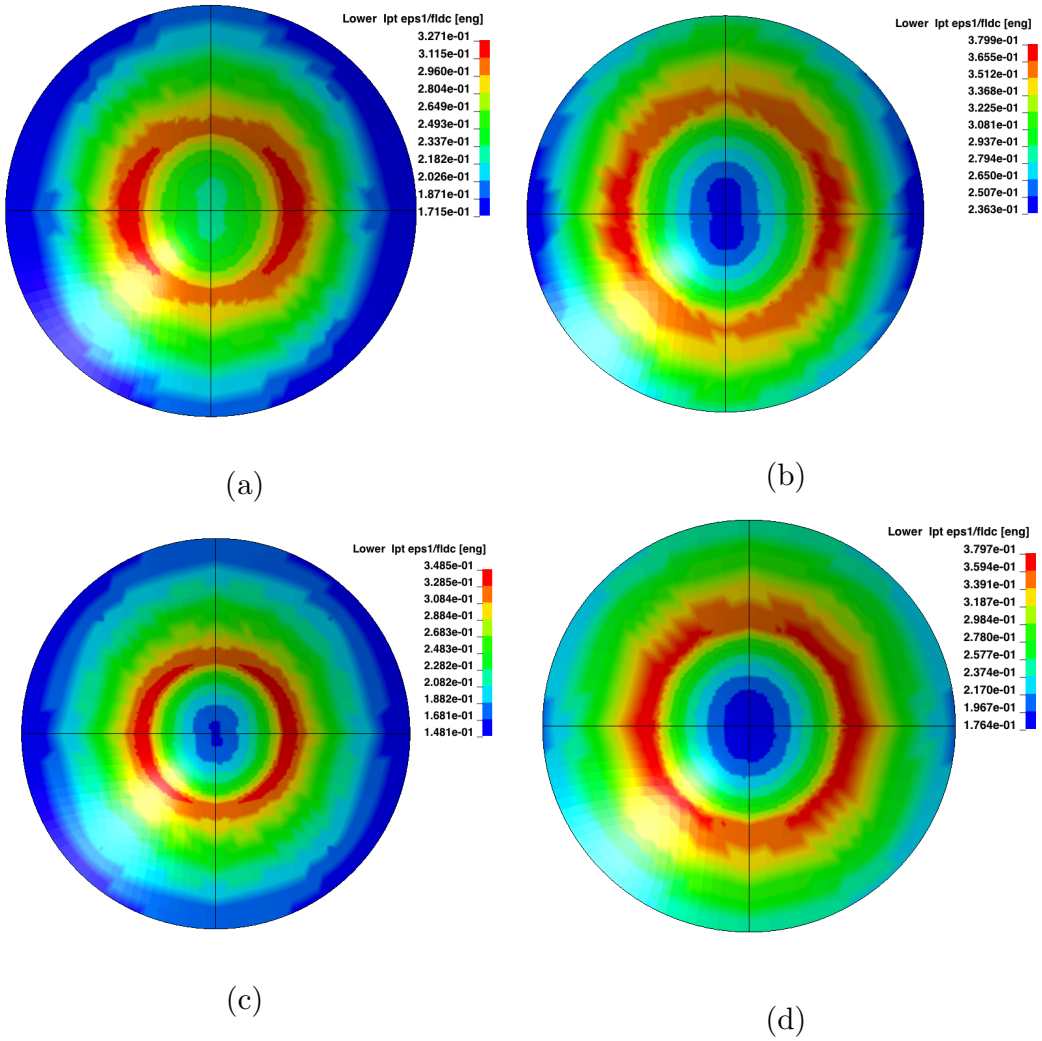

Fig. 18. Computed distribution of first principal strain in biaxially deformed (a,b) Celgard 2075; and (c,d) Celgard 2325.

Conclusions

We demonstrated the capability of replicating the deformations characteristic of indentation of battery module using the new experimental setup which places the pouch cell into specially designed enclosure with deformable medium replicating the response of the battery module. In this manner, we can study strains and failure in the top cell under large displacements which cannot be achieved in the traditional setup where the cell is tested against the non-deformable support. In the latter case, significant compressive stresses and strains can lead to internal short circuit induced by an electrode particles penetration through separator.

Experiments on cell stacks and cells supported by compliant backing reveal failure of the top cells by cracks always oriented with the normal parallel to the cell tabs. This direction corresponds to the machine direction of polyolefin separators processed by dry stretching. This indicates possibility for the anisotropy of mechanical properties of separators to influence the final mode of cell failure. In order to study the details of separator behavior, biaxial tensile experiments have been performed and distribution of strains was recorded using digital image correlation. In these experiments separators failed by straight cracks oriented along machine direction, thus confirming the observations from experiments on cells. The critical principal strain corresponding to the failure was measured as approximately 34% for Celgard 2325. This strain was independent of the indenter size. The finite element analysis with the model for separator behavior based on Barlat's model was able to capture the locations of principal strain maxima as well as the numerical values of the first principal strain.

Overall, the method being developed in this study is promising for applications involving assessment of battery safety where deformations representative of the module or pack are desirable; in our setup, such deformations can be achieved by testing one cell and replacing the rest of the module with deformable representative material (ballistic clay). This increases the safety of battery certification procedures and also subjects the battery cell to conditions that would develop in a battery pack under external mechanical loading.

References

[1] Goodenough, J.B., Kim, Y., “Challenges for rechargeable Li batteries,” Chemistry of Materials, 22-3, 2010, 587-603.

[2] Hollmotz, L., Hackmann, M., in: 22nd International Technical Conference on Enhanced Safety of Vehicles (ESV), (2011) 11-0269.

[3] National Highway Traffic Safety Administration (2006). “Electric Powered Vehicles: Electrolyte Spillage and Electrical Shock Protection”, FMVSS No. 305. U.S. DOT.

[4] Kai, X., Xueping, W., et al. (2014). “Comparative research on standards and regulations of electric vehicle post crash safety requirement_Transportation Electrification Asia-Pacific” (ITEC Asia-Pacific), 2014 IEEE Conference and Expo.

[5] SAE International (2014). "Recommended Practice for Electric, Fuel Cell and Hybrid Electric Vehicle Crash Integrity Testing” SAE J1766.

[6] SAE J2464-200911 (2009). “Electric and Hybrid Electric Vehicle Rechargeable Energy Storage System (RESS) Safety and Abuse Testing.” SAE International, Revision 11/06/2009.

[7] SAND 2005-3123 Technical Report (2005). “Freedom CAR Electrical Energy Storage System Abuse Test Manual for Electric and Hybrid Electric Vehicle Applications.” By Doughty, D., and Crafts, C., Sandia National Laboratories http://prod.sandia.gov/techlib/access-control.cgi/2005/053123.pdf

[8] Sahraei, E., Meier J., and Wierzbicki, T., “Modeling abd short circuit detection of 18650 Li-ion cells under mechanical abuse conditions,” Journal of Power Sources, 220, (2012) 360-372.

[9] UL 1642 Standard for Li Batteries, UL, 5, 2012-03-13.

[10] "1625-2008 - IEEE Standard for Rechargeable Batteries for Multi-Cell Mobile Computing Devices." IEEE SA -. Web. 20 Jan. 2015. http://standards.ieee.org/findstds/standard/1625-2008.html

[11] Keyser, M., Long, D., Jung, Y.S., Pesaran, A., Darcy, E., McCarthy, B., Partrick, L. and Kruger, C., in: Advanced Automotive Battery Conference (AABC), January 25-28, 2011, Pasadena, CA

[12] Takata, R., McCoy, C., Ofer, D., Stringfellow, R., Barnett, B., and Sriramulu, S., Proceedings of 44th Power Sources Conference, Curran Associates, Inc. Red Hook NY, (2010) p12

[13] Hatchard, T.D., Trussler, S., Dahn, J.R., “Building a "smart nail" for penetration tests on Li-ion cells,” Journal of Power Sources 247 (2014), 821-823.

[14] Lamb, J., Orendorff, C.J., “Evaluation of mechanical abuse techniques in lithium ion batteries,” Journal of Power Sources 247 (2014), 189-196.

[15] W. Cai, H. Wang, H. Maleki, J. Howard, E. Lara-Curzio, “Experimental simulation of internal short circuit in Li-ion and Li-ion-polymer cell,” Journal of Power Sources, 196 (2011) 7779-7783

[16] Maleki, H., Howard, J., “Internal short circuit in Li ion cells,” Journal of Power Sources 191 (2009), 568-574.

[17] Sahraei, E., Hill, R., Wierzbicki, T., “Calibration and finite element simulation of pouch lithium-ion batteries for mechanical integrity,” Journal of Power Sources, 201 (2012) 307-321

[18] Wierzbicki, T., Sahraei, E., “Homogenized mechanical properties for the jellyroll of cylindrical lithium-ion cells,” Journal of Power Sources, 241 (2013) 467-476

[19] Spotnitz, R., Muller, R., “Simulation of abuse behavior of lithium-ion bateries,” The Electrochemical Society, Interface, 12 (2012) 57-60

[20] Baldwin, R.S., Bennett, W.R., Wong, E.K., Lewton, M. R., Harris, M.K., Battery separator characterization and evaluation procedures for NASA’s advanced lithium-ion batteries, NASA/TM – 2010 – 216099.

[21] Kalnaus, S., Kumar, A., Wang, Y., Li, J., Simunovic, S., Turner, J.A., Gorney, P., “Strain distribution and failure mode of polymer separators for Li-ion batteries under biaxial loading,” Journal of Power Sources 378 (2018), 139-145.

[22] Marissen, R., “Craze growth mechanics,” Polymer 41 (2000), 1119-1129

[23] Zhang, S.S., “A review on the separators of liquid electrolyte Li-ion batteries,” Journal of Power Sources 164 (2007), 351-364.

[24] Arora, P., Zhang, Z., “Battery Separators,” Chemical Reviews 104 (10) (2004), 4419-4462.

[25] "LS-DYNA Keyword User’s Manual Volume II Material Models” Version 04/06/16 (r:7556), Livermore Software Technology Company, Livermore, CA, April 2016

[26] Lai, W.J., Ali, M. Y., and Pan, J., "Mechanical behavior of representative volume elements of lithium-ion battery cells under compressive loading conditions," Journal of Power Sources, 245 (2014), 609-623.

[27] Barlat, F., Lian, J., “Plastic behavior and stretchability of sheet metals. Part I: A yield function for orthotropic sheets under plane stress conditions,” International Journal of Plasticity 5 (1989), 51-66.

Appendix A: Experimental and simulation parameters

Table A1. Cell dimensions and nominal capacity*

Manufacturer	Cell width, *mm*	Cell height, *mm*	Tab height, *mm*	Cell thickness, *mm*	Nominal Capacity, *Ah*	Nominal Voltage, *V*
LG Chem	150	200	10	5.48	15 Ah	3.7

**Note: Battery pack was received in completely discharged state*

Table A2. Material constants for Barlat's 3-parameter plasticity model (MAT-36)

Variable	Description	Value
RO	Mass Density	1.00e-6 Kg/ mm^3
E	Elastic Modulus	0.5 GPa
PR	Poisson's Ratio	0.3
HR	Load curve in three directions	7
P1	Load curve in 45 degree direction	Average of MD and TD direction values
P2	Load curve in 90 degree direction	TD direction Stress Strain curve
m	Exponent in Barlat's Yield Surface	2.0
r00	Lankford parameter in 0 degree direction	1.0
r45	Lankford parameter in 45 degree direction	1.0
r90	Lankford parameter in 90 degree direction	1.0
lcid	Load curve in 0 degree direction (MD)	MD direction Stress Strain curve
aopt	Material Axis option is Global Orthotropic	2

Appendix B: Procedures for EV battery pack disassembly

Two Battery packs were delivered to ORNL in 2016. The packs were disassembled at R151 in Building 4500S. This lab was designated for battery pack disassembly. Prior to the arrival of the packs, safety walk through was conducted with the ORNL team. A basic Research Safety Statement (RSS) was develop for specific tasks and approved.

B:1. Disassembly of 2013 FORD Focus EV battery pack

FORD Focus EV pack arrived ORNL shipping in the summer of 2016 and two crates were delivered to the lab. As prior information indicated the battery pack was divided into two separate sub-units and disconnected to each other. The crates were well packaged and secured. No visible damage was observed. One of the crates was too big to get through the lab door. We got confirmation that the pack should be totally discharged and the actual pack should be able to through the door. The smaller crate was moved inside the lab and the large one was uncrated in the hallway. Figure 19 shows three set of picture of the crates, uncrated subunits with shrink wraps and exposed sub-units.

On the outside cover of subunit #1, there was a statement written in white paint: “Discharged and Shorted 4-10-2013”. The electricians were able to confirm from the outside connectors that there was no voltage measured from the terminals. After the verification, the electricians proceeded to open up the outside steel casing. According to the procedures, we assumed the inside battery pack could still be energized and once the casing was removed, all the terminals were measured to verify that the battery pack was not charged. As shown in Fig. 19 the battery pack was exposed with connections to the modules and battery management system (BMS) located on top of the modules. The electricians visually verified how the modules and BMS sensor wires were connected together and proceeded to take apart the battery pack. At that point, the safety boundary was removed; the PPE requirements for the electricians were safety glasses, no jewelries and gloves when necessary, as shown in Fig. 20.

Fig. 19. 2013 FORD Focus EV batteries packs out of crate

Fig. 20. 2013 FORD Focus EV batteries with steel casing removed

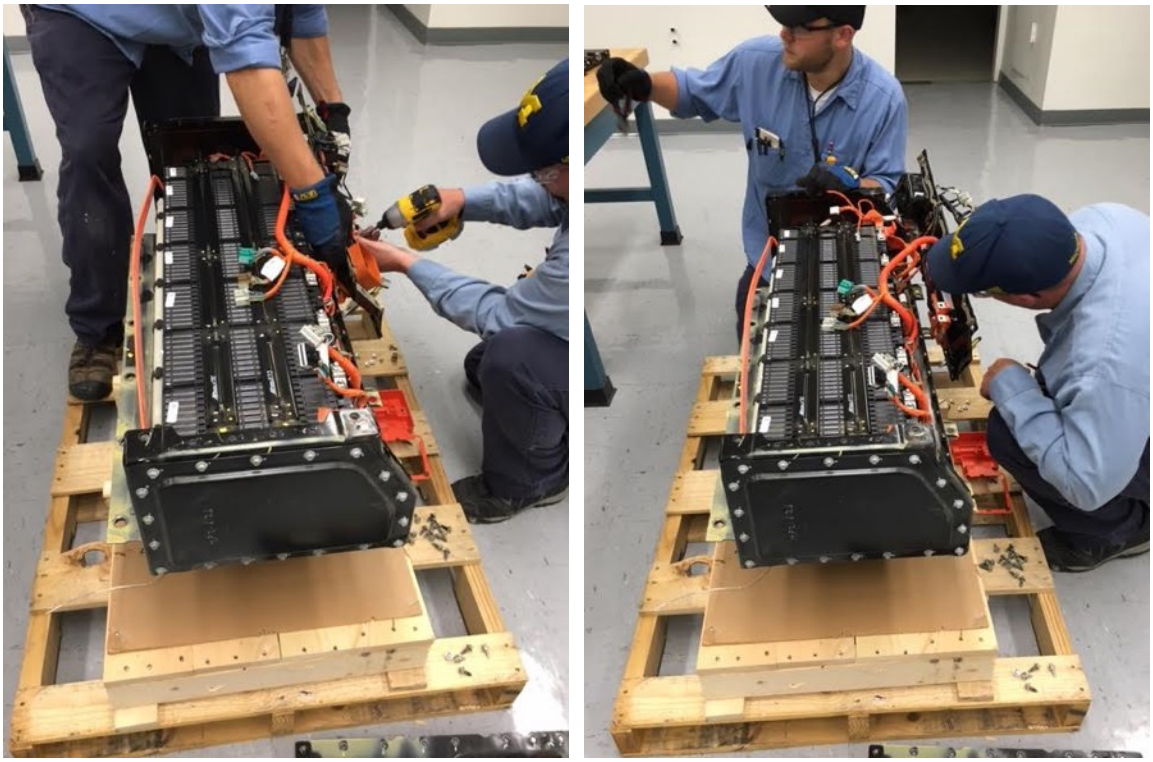

Fig. 21. PPE requirement of electricians were relaxed when the pack was verified with no charge

Figure 22 shows a close-up of the BMS system and cooling system inside the battery pack. Most of the connectors can be removed manually without cutting wires. The cooling system was disconnected and drained. We overserved residual coolants trapped inside the system and cooling plates. The coolants were regular engine coolants in commercial vehicles and were cleaned up when drops dripped out. The white plastic connectors in Fig. 22 connected all cooling plated in parallel and series. They must be removed before each individual module could be isolated.

Figure 23 shows images of the other sub-unit before and after the cover was removed. The same procedure was carried to verify that unit was not changed. The inside lay out, BMS connections and module connections were identical to the other subunit. The same procedure were used to disassemble the unit into modules. Figure 24 show an image of 11 and one-half modules after moving the BMS, cooling and connecting wires. They were mechanically secured by several bolted steel bars. Once that constrain was removed the modules started to expand and some of the module clip-on plastic casing started to snap indicating large compressive force existed in the system. The disassembly was completed within 3 hours.

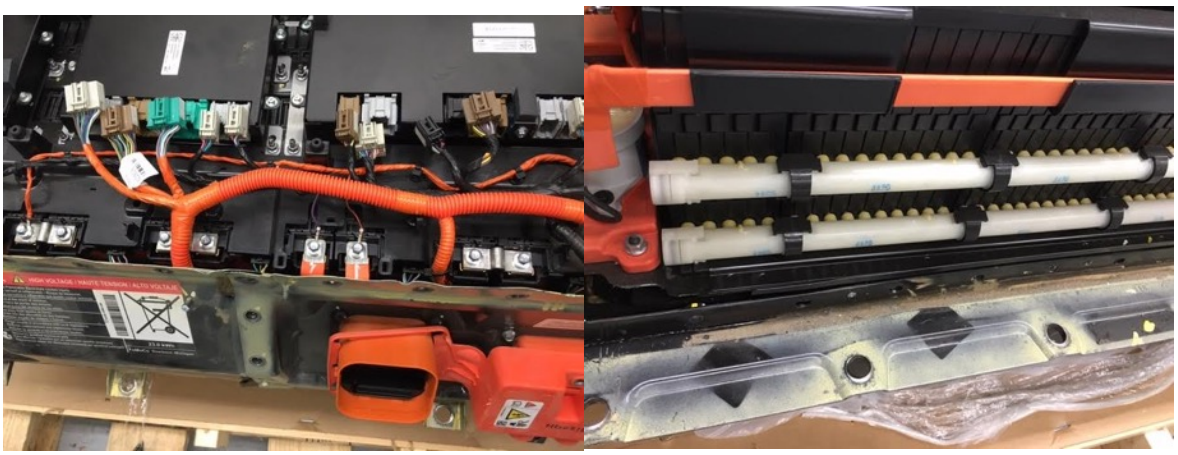

Fig. 22. FORD Focus sub-unit with BMS and cooling system

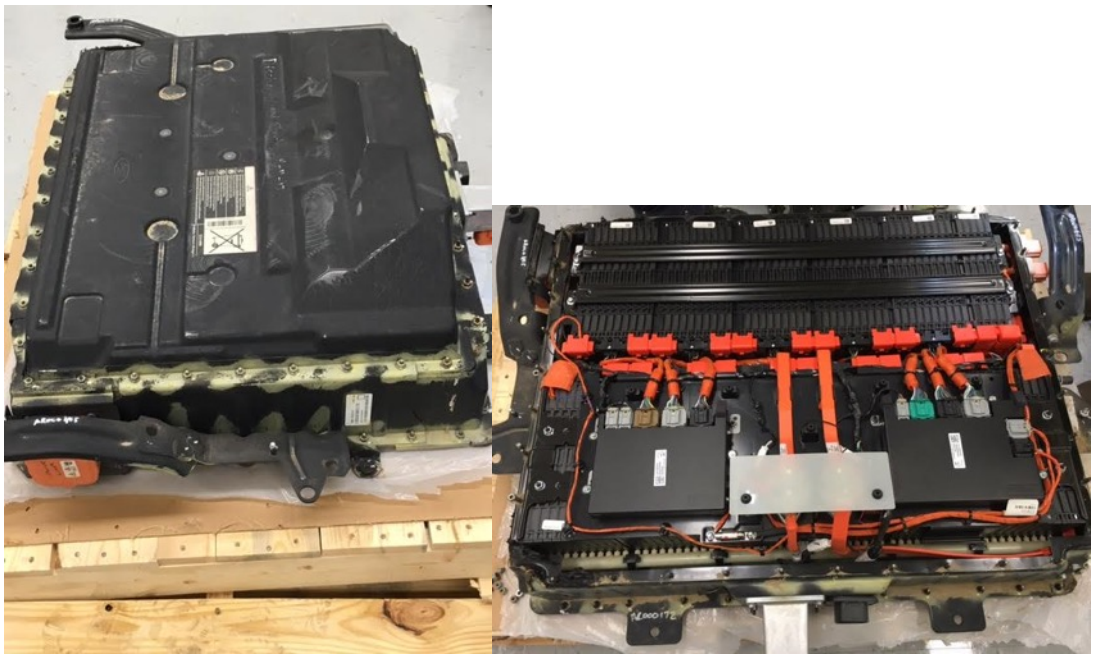

Fig. 23. FORD Focus EV subunit #2

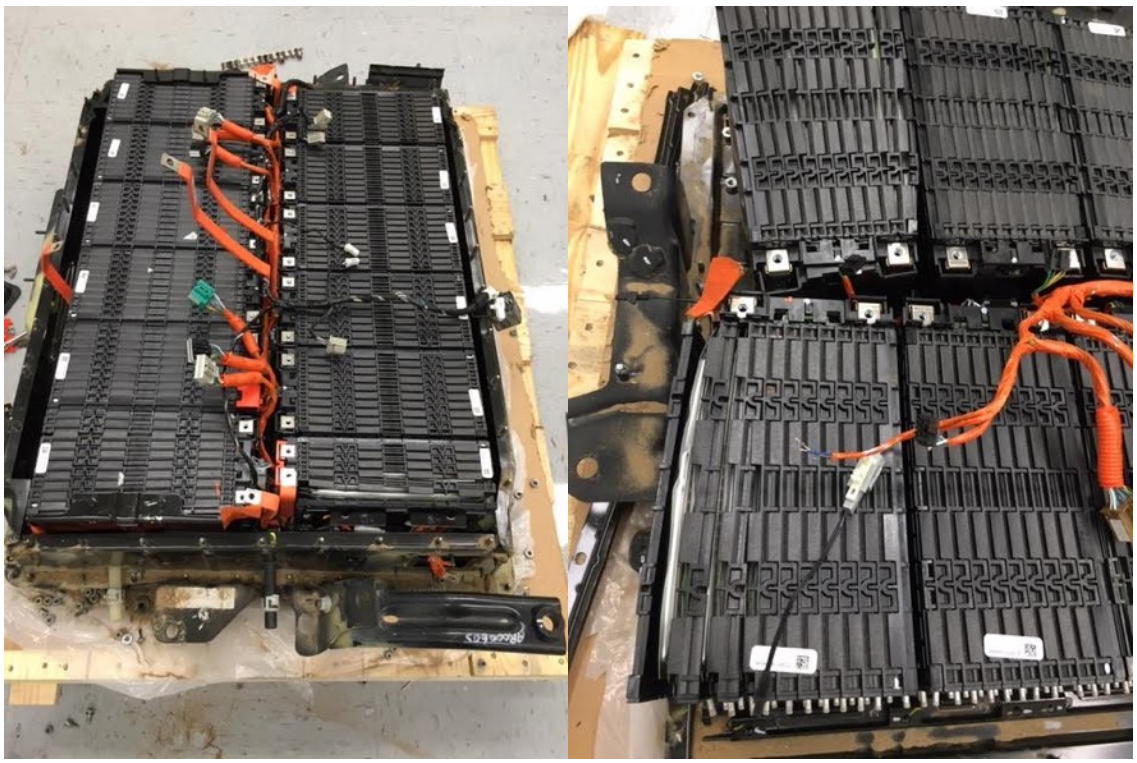

Fig. 24. Sub-unit #2 showing expansion of cells after removing mechanical constrains.

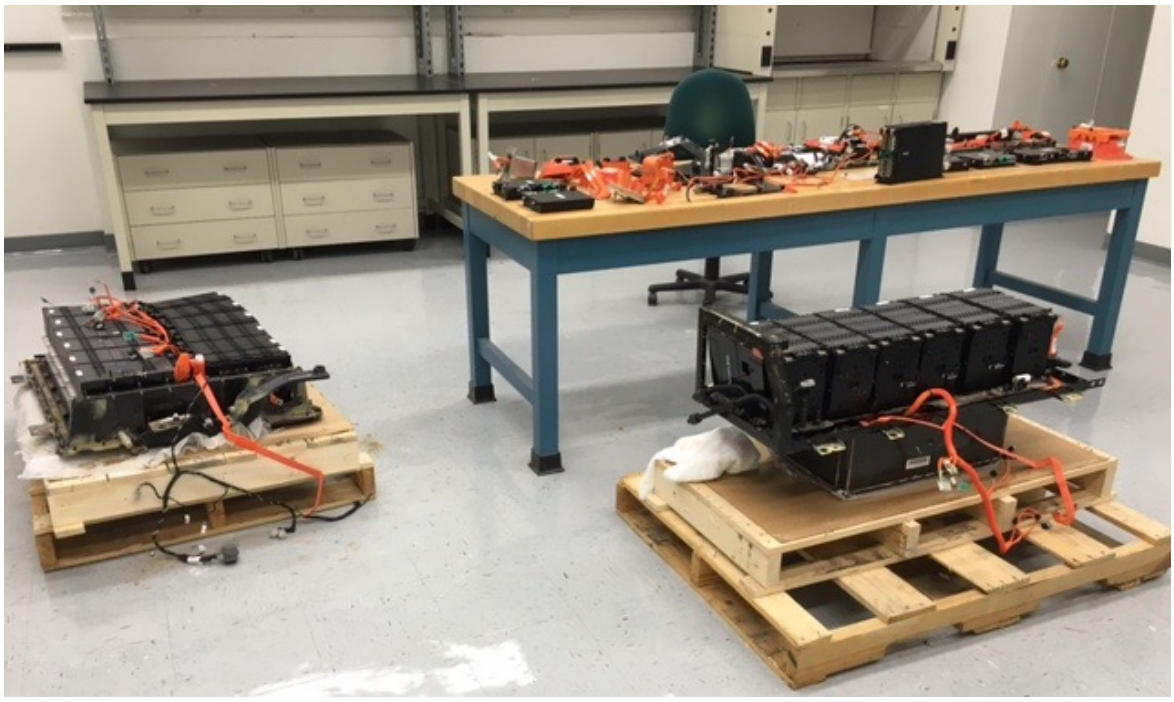

Fig. 25. FORD Focus battery pack in ORNL disassembly laboratory (R151 4500S)

B:2. Disassembly of 2013 Nissan Leaf battery pack

The Nissan Leaf EV pack arrived ORNL shipping around the same time. Before the delivery, ORNL shipping informed us that the single crate arrived with visible outside damage. As shown in Fig. 26, two holes were found on one side. We conducted visual inspection to make sure the steel casing inside had no visible damage. The shipping company was contacted to verify if the holes were observed during packaging. It was confirmed from the shipper, that they used scrap materials from other crates to build the one for the Nissan Leaf. The holes were "pre-existing" and not caused by damages during transportation. It was important to establish this confirmation and the pack was determined to be safe to deliver to the lab.

Fig. 26. Damaged crate of Nissan leaf battery pack

Fig. 27. Nissan Leaf pack in lab R151 and boundary set after the pack was confirmed still charged

Once the pack is delivered to the lab, we used the same procedures to open the crate to expose the pack. From the outside terminals no voltage was present. When the cover was opened and the electricians measured 128V at the connection point indicated at least half of the modules were still partially charged. Since this was inconsistent with the information given by the shipping company, the work was stopped immediately. We were told the pack was discharged and it appeared to be so from outside terminals. A boundary was set with red tape as shown in Fig. 27. We had to switch to the plan that deals with energized packs.

The procedures for energized packs required further reviews and approvals from the operation divisions. We waited until the new procedure was approved to resume the disassembly process. As shown in Fig. 28, the new procedure required different PPE for the electricians. They must wear hardtop hats, use face shields, and rubber gloves. Insulated tools were required as well. They were able to open the case, remove the BMS connections and controller. They visually identified the main connection buses and confirmed with supervisor on their observations. Then they proceeded to break apart the serial connected modules into half capacity and smaller units. During the process, we found all the modules in the pack were still energized and open circuit voltage was 6.5V in each module.

Figure 27 shows a close-up view of the pack with BMS removed. The individual modules were removed and taken out. Fig. 28 also shows an image with all 48 modules removed. All the terminals were taped and insulated to avoid accidental contacts and external short circuit. The Nissan Leaf pack has no cooling system. The disassembly was easier and completed within two hours.

Fig. 27. New PPE requirements for energized pack disassembly

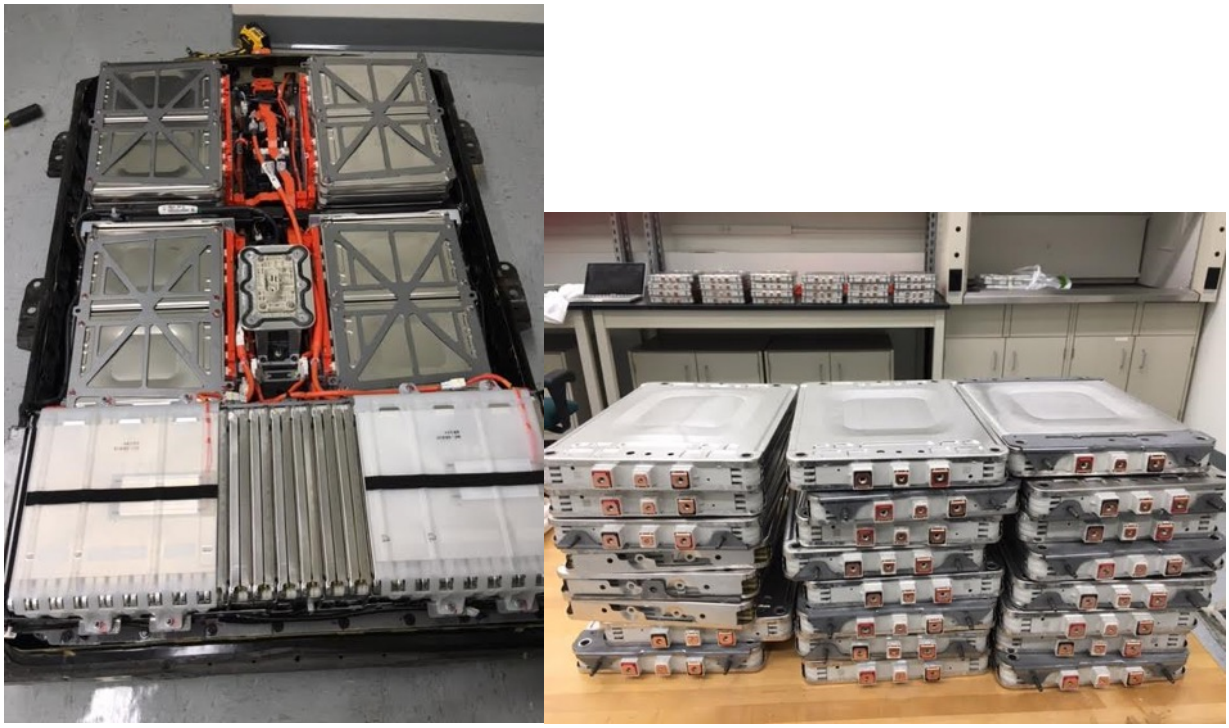

Fig. 28. Close-up look at the modules and disassembled modules

B:3. Disassembly of 2013 FORD Focus EV Modules

The FORD focus modules were not charged. Figure 29 shows an image of a half module and a full module with cooling connectors removed and plastic casing partially snapped. The cycled cells inside the modules were under large pressure. The force was large enough to open the plastic cases which were clipped together. Because the tabs of the cells were still welded to the connectors, the case opened up from the back. The following steps were used to disassemble the module:

- Use a flat screw driver to open up the clipped-on plastic panels and frames.
- Remove the aluminum cooling plates by pulling them out of the package
- Open up the front cover to expose the connectors and ultrasonically welled tabs
- Use a plier and wire cutter to disconnect the tabs from the connector brackets
- The loosened cells can be pulled out from the back one by one
- Since we were dealing with totally discharged cells, no insulated tools were required. For charged cells, extra caution is needed not to short out the terminals and cause external discharge (sparks or heating may occur)

Figure 30 are images of a half module before and after disassembly. Figure 31 are disassembled cells and cooling plates of a full module and a half module. As mentioned, the half module contained ten 15 Ah cells in 5P-2S connection configuration. The full module contained twenty 15 Ah cells in 5P-4s configuration. Each cell has at least one surface in contact with an aluminum cooling plate.

Fig. 29. FORD Focus EV half module and full module

Fig.30. A half module before disassembly and after assembly

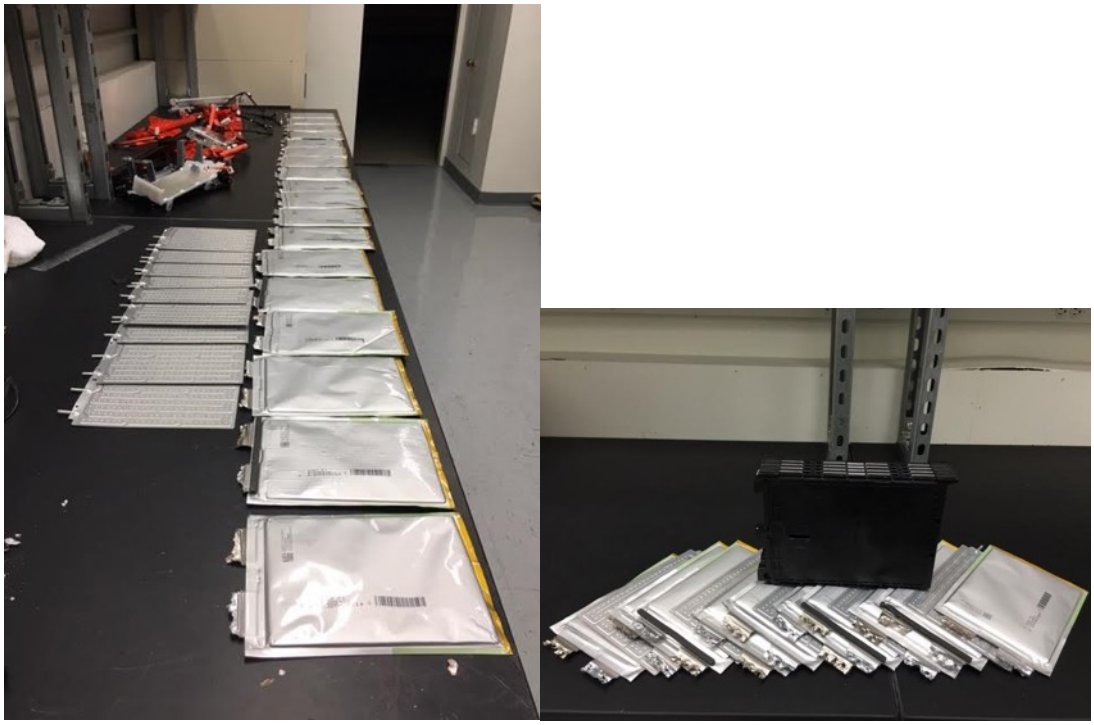

Fig.31. FORD Focus battery pack in ORNL disassembly laboratory

B:4. Disassembly of 2013 Nissan Leaf Modules

Nissan Leaf modules are shown in Fig. 32. The terminal marked in Red is positive and Black for negative. The middle terminal was used for BMS voltage monitoring. Since all the modules were partially charged, their terminals were insulated with clear tapes and only removed for connection. Figure 33 shows a module with top cover removed showing the plastic frames and connectors. The 2P-2S configuration was observed. Since the module does not have any cooling system only cell removal is needed. Figure 34 is the disassembled top cover and the exposed cells.

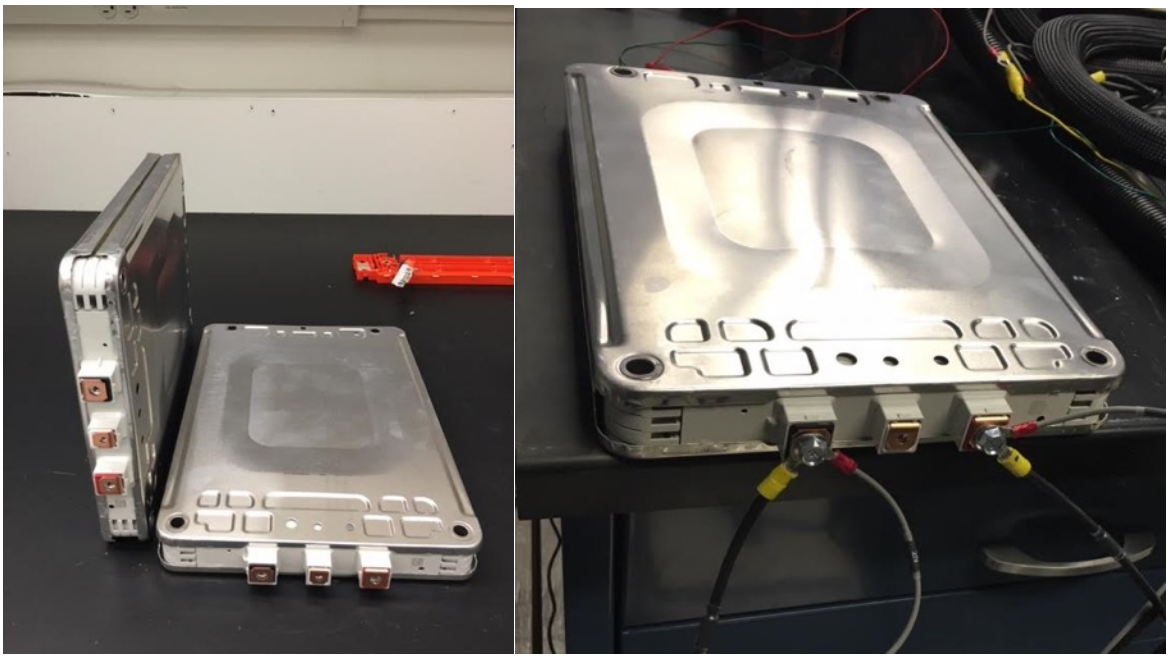

Fig.32. Nissan Leaf modules and electrical connections

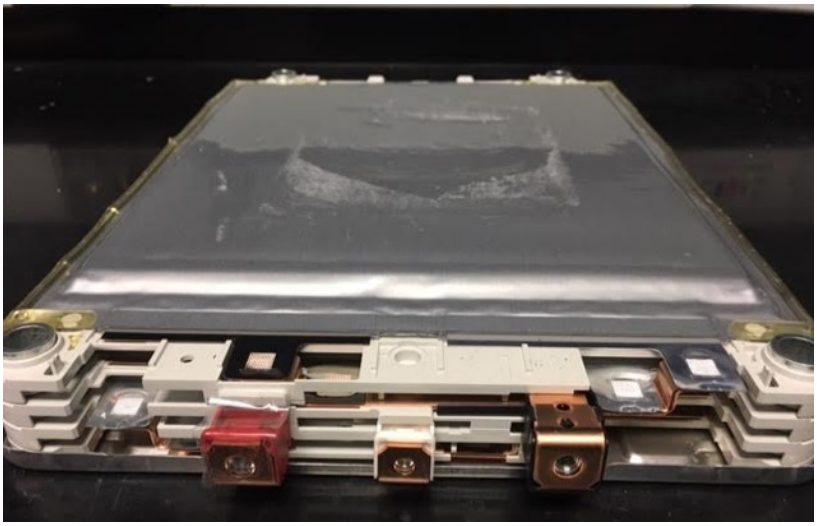

Fig.33. Nissan leaf module with top removed

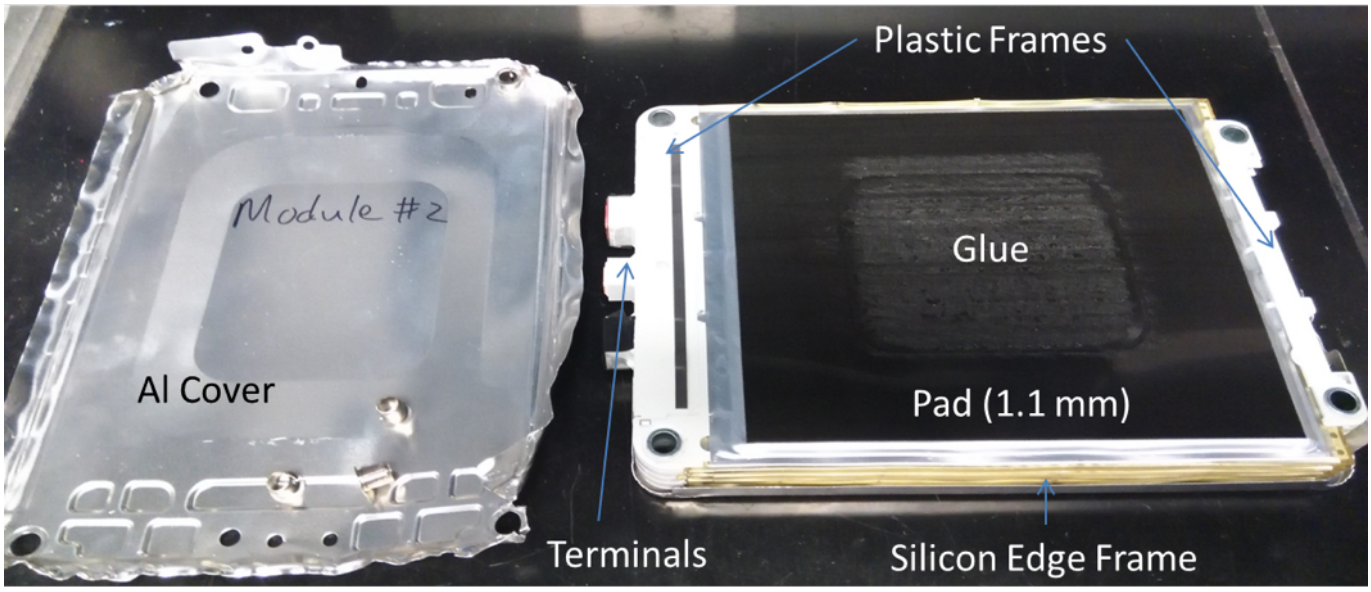

Fig.34. Nissan Leaf module parts

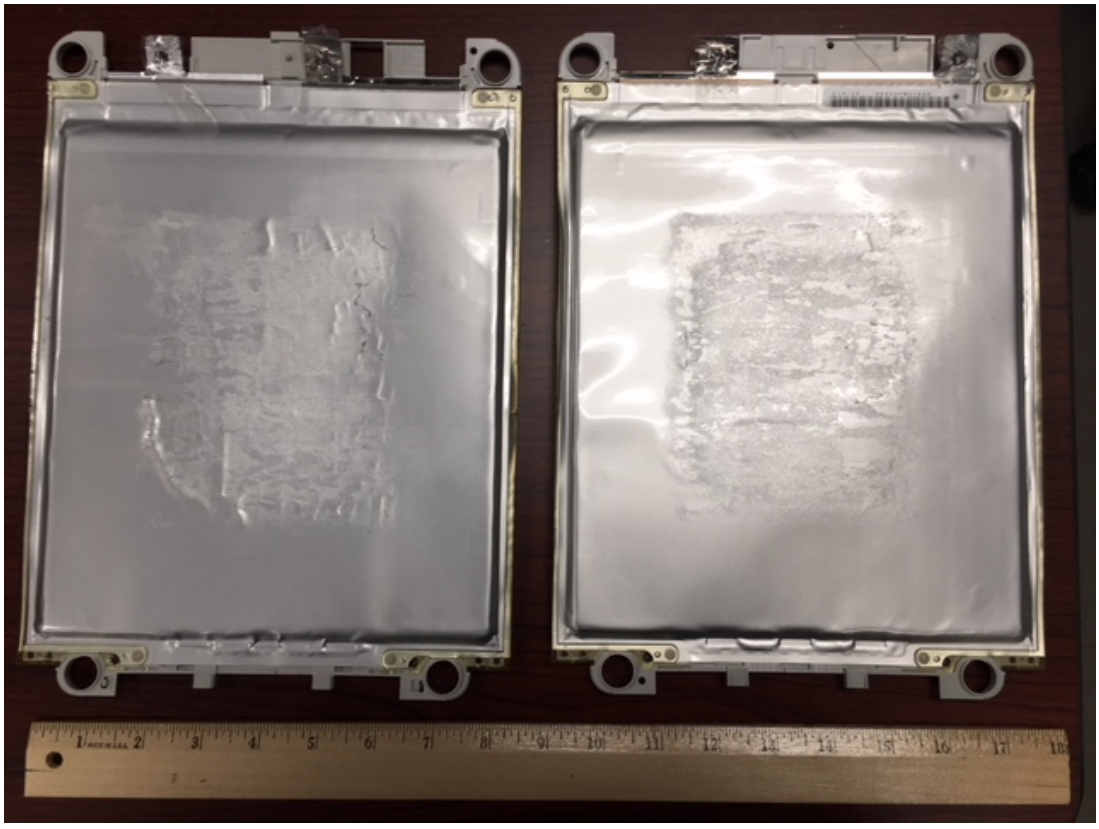

Fig. 35. Disassembled Nissan Leaf single cells

The 2P-2S connections of the module could be further disassembled by separating the ultrasonically welded anode and cathode tabs. It is important to avoid crossing the connectors during this step for external short circuit. Once the terminals are disconnected, insulating tapes need to be put on to electrically isolate them. Since the cells are glued together with the same adhesive, separating the cells is the next step. The best practice is to put a few drops of acetone between the cells and wait a minute or so to let the glue dissolve. It is helpful to use a thin sheet

of plastic, such as a plastic ruler; to push down and separate the cells. Since the cells are flexible, they can be easily bent and folded. It is not recommended to use force to separate them even when the glue is partially dissolved. It is recommended to use several steps to completely dissolve the glue and separate the cells using minimum force. Figure 35 is an image of two disassembled cells.

The following procedures were used to disassemble the charged Nissan Leaf module:

- The terminals need to be insulated with electric tape
- Insulated tools need to be used and contact between metal terminals, tabs and wires need to be avoided
- Use a plier to open the top aluminum cover. The cover is glued to a rubber pad. Applying some acetone to the interface will soften the glue and help to break the bonding
- The pad is glued to the cells and similar procedure is need to break the bonds
- Metal connections and plastic frames need to be removed to separate the cells

Use acetone and a thin plastic tool to dissolve glue and separate the cells

Appendix C: Post-mortem analysis of pouch cells

The 2013 Focus cells were completely discharged to 0V upon shipment. All the cells were inflated due to the gas released from the cell materials. Here are the specific test conditions;

- Cells were discharged before testing
- Right before the indentation tests, pouch of the cells were punctured to release gas
- After the indentation, cells were opened and left over a weekend in the hood to dry

Figure 36 shows images of the separator and electrode when the cell was opened up. The top layer of the separator was stretched and showed a clear line in the middle. However, it was not punctured and there was no crack. The electrode under the top separator showed a large crack. A closer look under the crack in Fig. 37 showed that the same crack went through multiple layers and the separator was sheared along the same fault line. The color of the electrode indicated the effect of long term aging and storage after discharge.

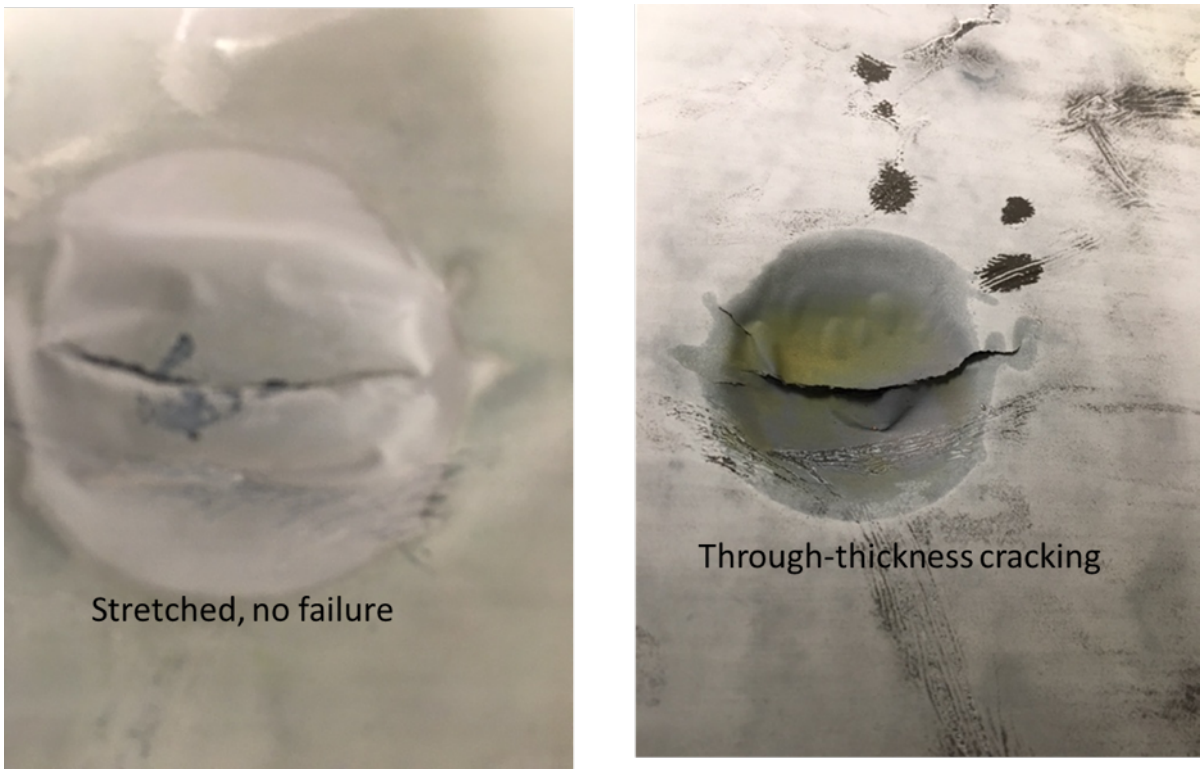

Fig.36. Separator and electrode in Cell #1 of the 10-cell stack

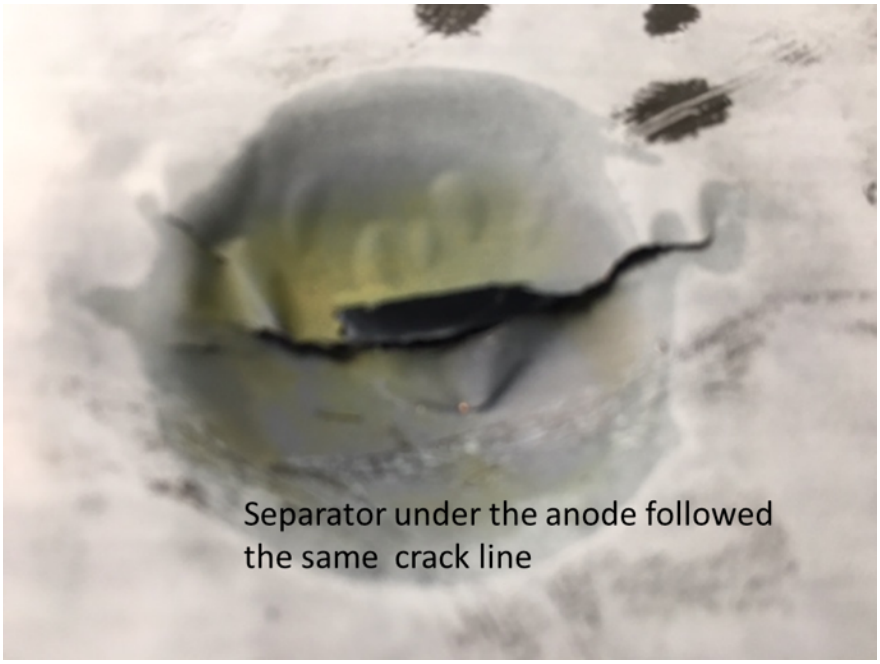

Fig.37. A closer look at the large through-thickness crack.

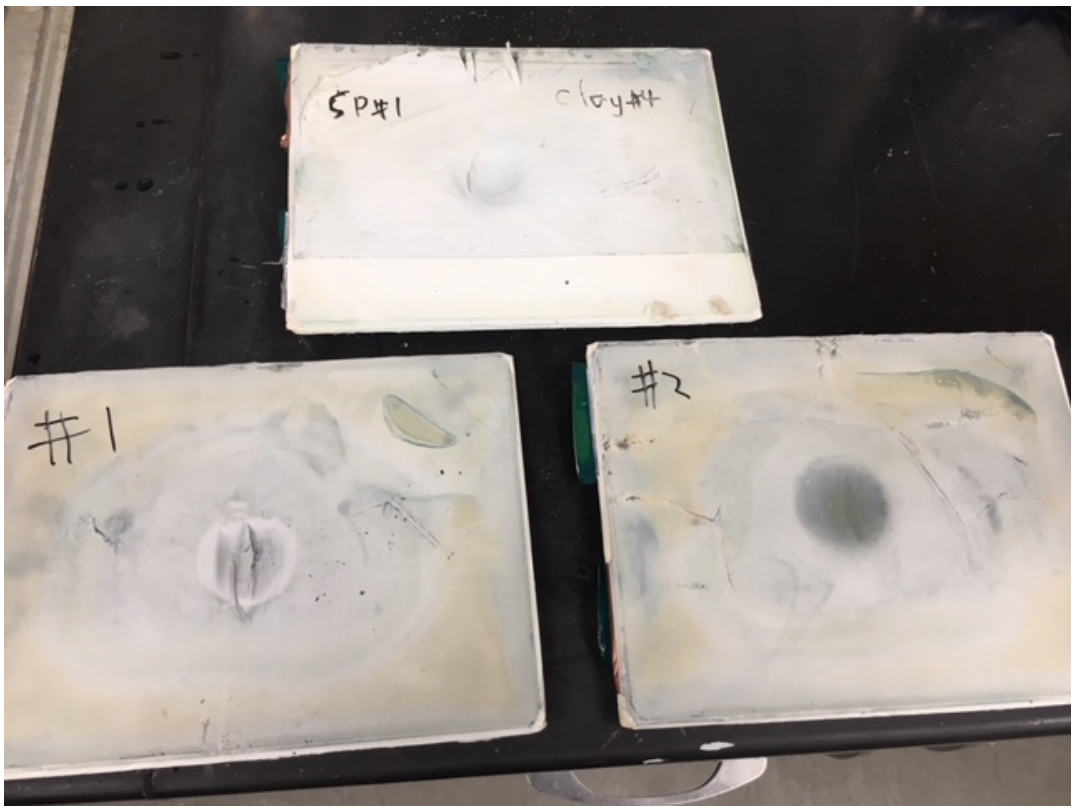

Fig.38. Top separator layer under the pouch of the three cells

Similar wrinkle was observed on the clay-back cell and cell #1 of the 10 cell stack, as shown in Fig. 38. No wrinkle was observed in the 2nd cell of the 10 cell stack. The dark circle indicated thinning of the separator. In all three cases, the top separator was not cracked.

When the top layer was removed the rest of the stack is shown in Fig. 39. As a first observation, there were lots of deposits on the anode surface. In fact, it seemed to be a white coating on the surface with impressions of the cooling plate patterns. When the first layer of anode was removed, it appeared to be very brittle. Cracking and fractures occurred when the corners of the electrode were lifted. In some cases, only a portion of the electrode could be separated. More deposits were observed on the backside and the lifted anode showed a very clear pattern of the cooling plate.

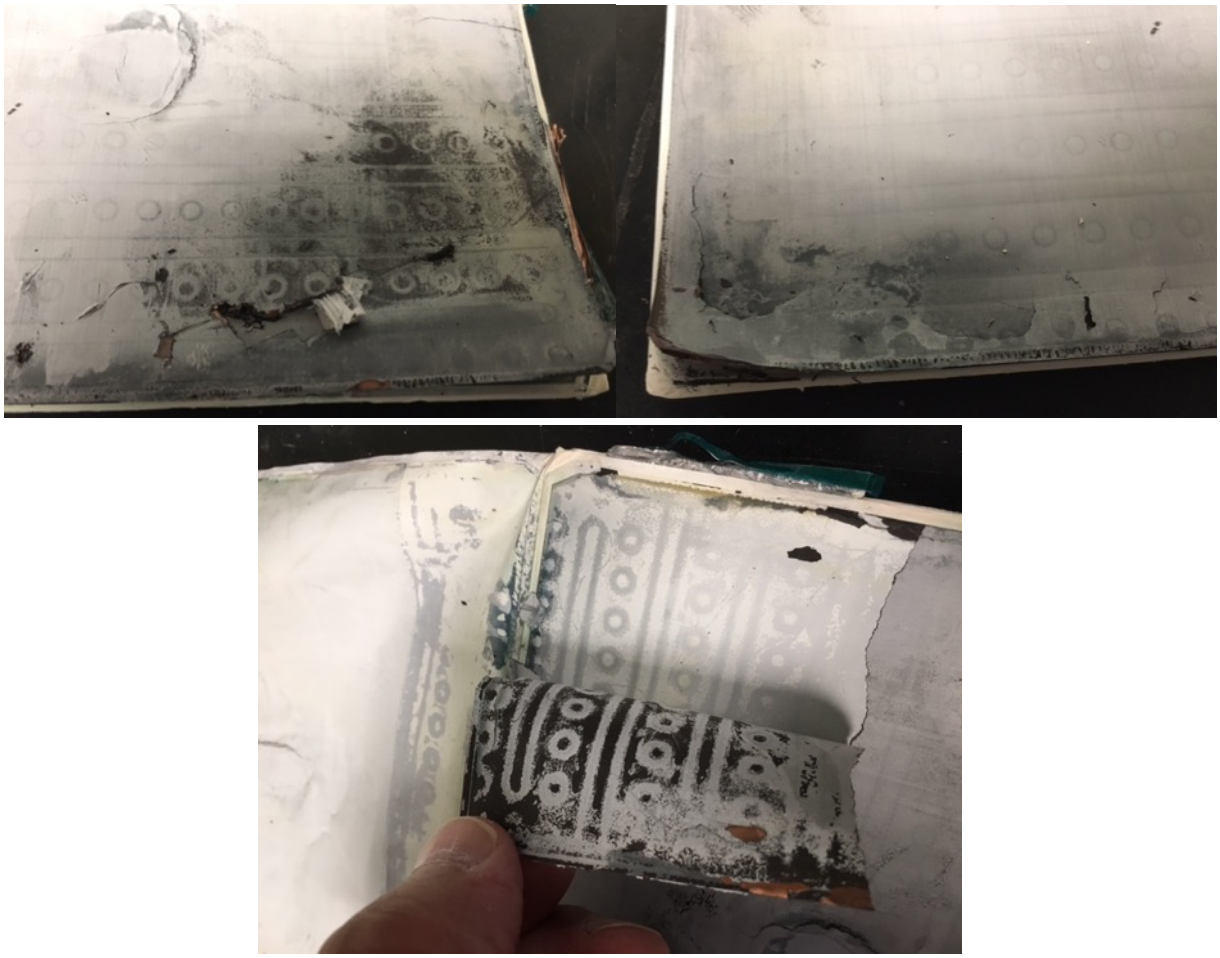

Fig.39. Brittle anodes

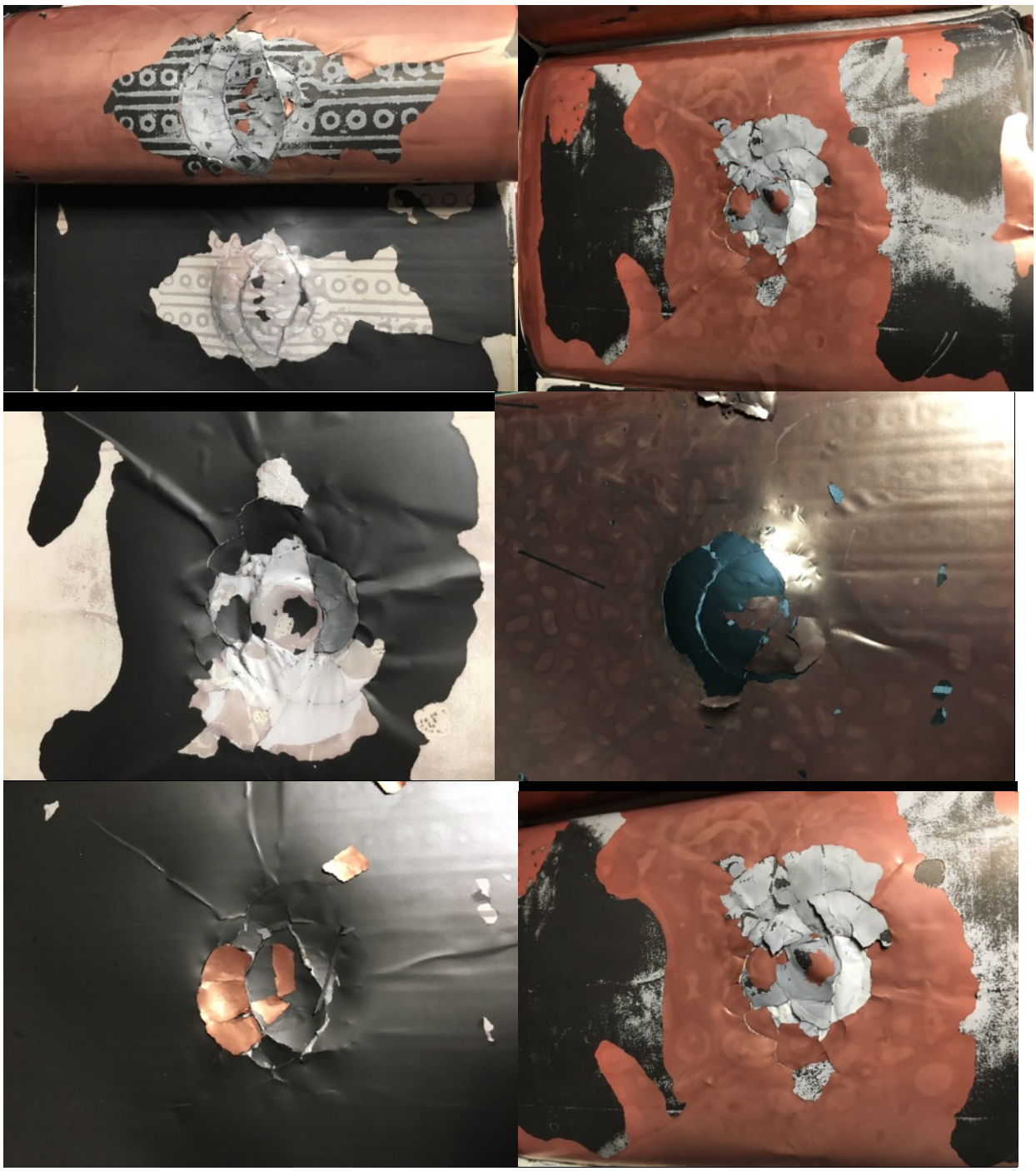

Fig.40. Images of electrodes

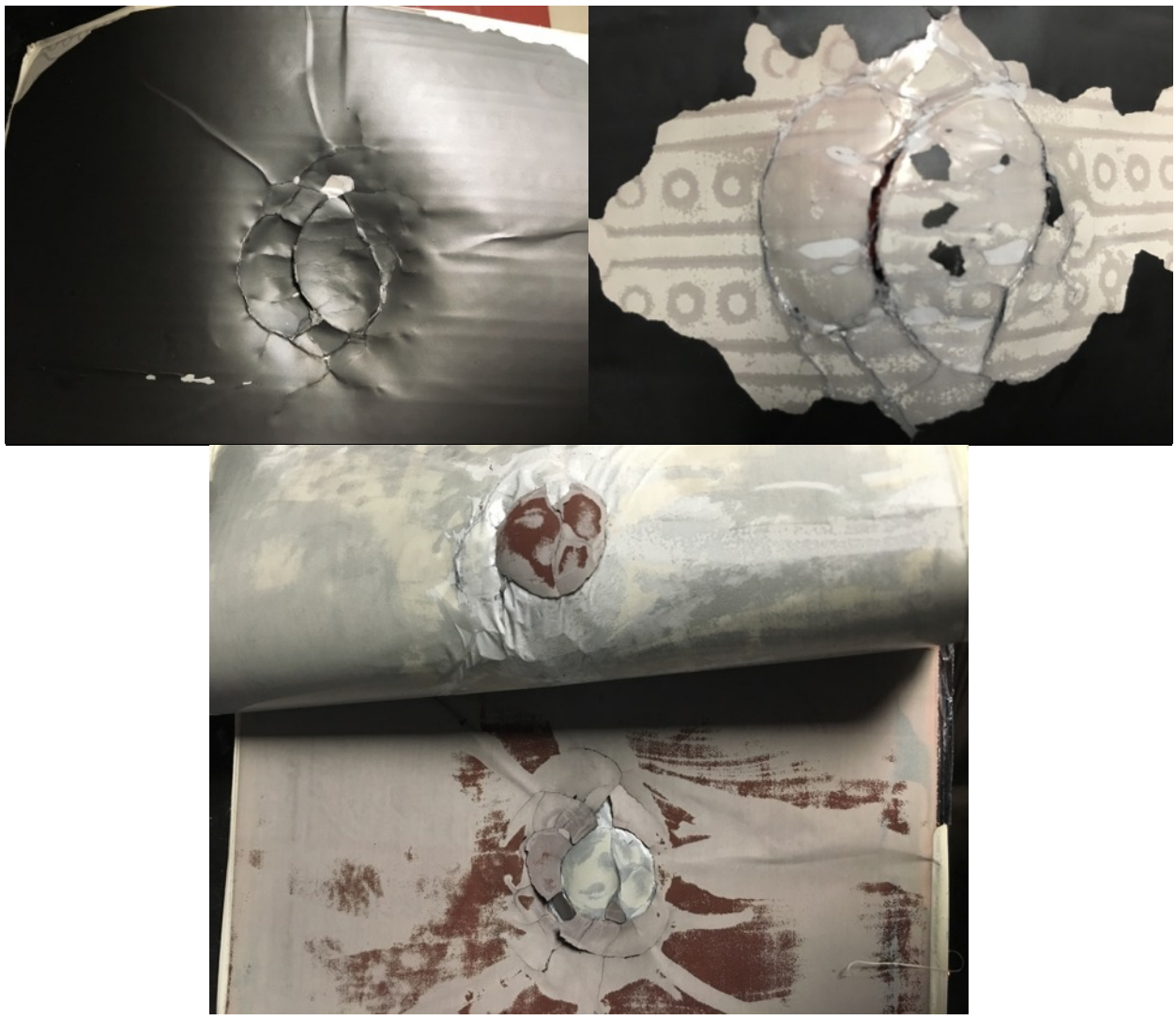

Fig.41. Images of cathode failure under the indenter

Figure 40 are images of electrodes. Figure 41 showed three images cathode failure. The following observations were made:

- The anodes were brittle and broken into pieces under the indented areas
- The anodes fracture pattern was different from the cathode facture pattern
    - Anode: more fragmentation under the indenter
    - Cathode: large cracks across the indented area

Overall, the post-mortem exams were also destructive although they revealed some critical insights of the failed cells. Non-destructive techniques such as 3D x-ray tomography could not be used for large batteries. However, special techniques and sample preparation methods can be developed to allow better inspection of the internal structure changes leading to the final failure.